

# Two-port CW measurements on RF cavities: Notes on self-consistency assessment and indirect methods

Walter H. Hartung, Wei Chang, Sang-Hoon Kim, Taro Konomi, Ting Xu

*Facility for Rare Isotope Beams, Michigan State University, East Lansing, Michigan, USA*

## Abstract

In the case of a radio-frequency (RF) cavity with a mismatched input coupler, a direct calculation of the power dissipation in the cavity and the intrinsic quality factor from continuous-wave (CW) measurements may have uncertainty due to systematic errors. Formulae for an indirect calculation of these quantities are derived for the case of a cavity with two couplers of fixed coupling strength. In this approach, the signal from the pickup coupler is used to infer the amplitude of the “emitted wave” from the input coupler. A graphical method for self-consistency assessment is evaluated. The impact of frequency offsets is considered. Applications of these methods are presented, drawing on cold tests of superconducting cavities produced for the Facility for Rare Isotope Beams.

## Contents

<b>1</b>	<b>Introduction</b>	<b>1</b>	<b>7</b>	<b>Applications and Examples</b>	<b>11</b>
<b>2</b>	<b>Background</b>	<b>2</b>	7.1	Dewar Tests: Real-Time . . . . .	11
2.1	CW Measurement Basics . . . . .	2	7.2	Dewar Tests: Final Analysis . . . . .	12
2.2	RF Power and Field Level Calibration . . . . .	3	7.3	Cryomodule Tests . . . . .	13
<b>3</b>	<b>CW Analysis</b>	<b>3</b>	<b>8</b>	<b>Conclusion</b>	<b>14</b>
3.1	Direct Method Using $P_f - P_r - P_t$ . . . . .	3	<b>Acknowledgments</b>	<b>14</b>	
3.2	Indirect Method Using $P_t/P_f$ : Brute Force Derivation . . . . .	4	<b>Appendix A</b>	<b>Analysis of Modulated Measurements</b>	<b>14</b>
3.3	Indirect Method Using $P_t/P_f$ : Emitted Wave Derivation . . . . .	4	Appendix A.1	Modulated Measurement Basics . . . . .	14
3.4	Indirect Method: Additional Formulae, Comments . . . . .	4	Appendix A.2	Weak Pickup Coupling . . . . .	15
<b>4</b>	<b>Graphical Assessment Method: Derivation</b>	<b>5</b>	Appendix A.3	Arbitrary Pickup Coupling Strength . . . . .	15
<b>5</b>	<b>Graphical Assessment Method: Vertices and Limiting Cases</b>	<b>6</b>	<b>Appendix B</b>	<b>Analysis of CW Measurements with Arbitrary Pickup Coupling Strength</b>	<b>16</b>
5.1	Weak Input Coupling . . . . .	6	Appendix B.1	Direct Method . . . . .	16
5.2	Unity Input Coupling . . . . .	6	Appendix B.2	Indirect Method . . . . .	16
5.3	Strong Input Coupling . . . . .	6	Appendix B.3	Graphical Assessment Method . . . . .	16
<b>6</b>	<b>Detuning</b>	<b>6</b>	Appendix B.4	Example: Cold Test with Approximately Equal Input and Pickup Coupling Strengths . . . . .	17
6.1	Graphical Assessment Method: Detuning Predictions . . . . .	6	<b>References</b>	<b>17</b>	
6.2	Graphical Assessment Method: Detuning Measurements . . . . .	7			
6.3	Quality Factor Calculation with Detuning: Predictions . . . . .	10			
6.4	Quality Factor Calculation with Detuning: Measurements . . . . .	10			

## 1. Introduction

Continuous-wave (CW) measurements are used to evaluate the performance of radio-frequency (RF) cavities. RF cavities are used in charged particle accelerators, among other applications. The cavity stored energy, field amplitude, accelerating gradient, and quality factor may be inferred from CW measurements. RF cavity testing is an important part of cavity development, surface preparation development, and cavity production for small- and large-scale accelerators.

For normal-conducting RF (NRF) cavities, single-port or multi-port measurements are commonly used. High-field testing may require a high-power amplifier and water cooling of the cavity exterior. Feedback may not be needed, as the bandwidth may be such that the amplitude and phase are relatively stable with an open-loop RF system.

For superconducting RF (SRF) cavities, 2-port measurements are typical. The cavity must be cooled to cryogenic temperatures, but usually the test can be done with a small amplifier (50 to 300 W being typical). Due to the narrow bandwidth, a phase-lock loop or a self-excited loop is typically used to ensure that the cavity is driven on resonance.

Methods for measurements on RF cavities and analysis of the results can be found in the literature, for example in Refs. [1–3]. Typically the cavity is modeled as an *LRC* circuit; though both a circuit model and a waveguide model for the cavity-coupler system are considered in Chapter 5 of Ref. [3]. Considerations specific to SRF cavity case are discussed in Chapter 8 of Ref. [2].

Systematic errors are generally present in RF measurements due to imperfect components and imperfect matching. The systematic errors may produce large errors in the inferred quantities if the input coupler is poorly matched to the cavity. A variable coupler may be used to minimize the input coupler mismatch, but such a coupler makes the system more complex, and there are sometimes concerns about increasing the risk of particulate contamination due to the materials and moving parts.

In the presence of systematic measurement errors, additional care is needed in the analysis of RF measurements. Methods to check the consistency of derived quantities are useful in assessing the impact of systematic errors and the validity of the results. A thorough understanding of systematic errors becomes particularly important in cavity development efforts oriented toward performance improvements with the need for precise performance comparisons between different cavity designs, different surface treatments, and so on. Some of these issues are discussed in recent papers on SRF cavity measurements, including an evaluation of the effect of an imperfect circulator or an imperfect dual-directional coupler; an error analysis for derived quantities; and error models with vector correction in lieu of scalar correction [4, 5].

In both the NRF and SRF cases, a basic analysis of CW measurements may be done via a “direct” approach: the power dissipation in the cavity is calculated from the difference between the forward power supplied by the RF system and the reverse power from the input coupler. However, in the 2-port case with fixed coupling strengths, CW measurements are over-determined, which allows for an “indirect” method to calculate derived quantities and allows us to check the consistency of the results.

This report describes the direct and indirect analysis methods, along with a graphical method to check the self-consistency of the measurements. The methods can be applied to 2-port CW measurements with fixed coupling strength for both NRF and SRF cavities. A weakly-coupled pickup coupler is assumed to simplify the derivation; for completeness, the case of arbitrary pickup coupling strength is considered in the appendices. Vec-

tor measurements are not needed to apply these methods.

The graphical methods described in this report have been applied to SRF cavity tests at Michigan State University (MSU) for a number of years. Work at MSU has included SRF cavity development, prototyping, and production for an ion accelerator linac [6] and the driver linac for the Facility for Rare Isotope Beams (FRIB) [7]. The latter effort required cold testing and certification of 324 SRF cavities [8]. Certification testing is done with close-to-matched input coupling and we generally use the direct method to infer the quality factor. An additional effort in the past several years has been oriented toward the development of multi-cell cavities for the proposed FRIB energy upgrade [9].

In more recent years, the MSU SRF team has begun developing techniques for in-situ plasma processing of FRIB cavities [10]. The plasma is driven with RF power via the fundamental power coupler (FPC), but the cavity is at room temperature. As a result, the FPC is weakly coupled. We have found that the indirect method is useful to infer the quality factor and power dissipation with plasma on, and to estimate the power transfer to the plasma [11].

This report describes the indirect and graphical methods in more detail and includes some examples based on SRF cavity testing at MSU. Some of the derivations were previously included in an appendix of a PhD dissertation by D. J. Meidlinger [12]. The present report includes a description of the “emitted wave” picture, which provided the original inspiration for the methods, but which was not previously documented. Limiting cases and the impact of frequency offsets are discussed as well.

## 2. Background

### 2.1. CW Measurement Basics

We may measure the following quantities in CW mode: the forward power ( $P_f$ ); the reverse power ( $P_r$ ); the transmitted power ( $P_t$ ); the resonant frequency ( $f_0$ ). These quantities are measured on resonance, with the drive frequency set for maximum  $P_t$  and minimum  $P_r$ . Derived quantities of interest include the stored energy ( $U$ ), the accelerating gradient ( $E_a$ ), the power dissipation in the cavity walls ( $P_d$ ), and the intrinsic quality factor

$$Q_0 \equiv \frac{\omega_0 U}{P_d}, \quad (1)$$

where  $\omega_0 = 2\pi f_0$  is the resonant angular frequency. Other useful quantities are the strength of the input coupler ( $Q_{ext,1}$ ) and the strength of the pickup coupler ( $Q_{ext,2}$ ). The latter can be defined straightforwardly as

$$Q_{ext,2} \equiv \frac{\omega_0 U}{P_t}. \quad (2)$$

Additional useful quantities are the coupling factors

$$\beta_1 \equiv \frac{Q_0}{Q_{ext,1}}, \quad (3)$$

$$\beta_2 \equiv \frac{Q_0}{Q_{ext,2}}. \quad (4)$$

Though we refer to  $Q_{ext,1}$  and  $Q_{ext,2}$  as coupling strengths and refer to  $\beta_1$  and  $\beta_2$  as coupling factors, others may use the opposite terminology. Using [Equation \(1\)](#) and [Equation \(2\)](#), we can express  $\beta_2$  as a power ratio:

$$\beta_2 = \frac{P_t}{P_d}. \quad (5)$$

We define the “scattering parameters”

$$|S_{11}| \equiv \sqrt{\frac{P_r}{P_f}}, \quad (6)$$

$$|S_{21}| \equiv \sqrt{\frac{P_t}{P_f}}, \quad (7)$$

which are typically measured on warm cavities at low power using a network analyzer, but can be obtained from power measurements as well.

Additional quantities of interest include the loaded quality factor  $Q_L$ , which can be calculated via

$$\frac{1}{Q_L} = \frac{1}{Q_0} + \frac{1}{Q_{ext,1}} + \frac{1}{Q_{ext,2}} \quad (8)$$

and the loaded bandwidth

$$\Delta f \equiv \frac{f_0}{Q_L} \approx \frac{f_0}{Q_0}(1 + \beta_1), \quad (9)$$

with the right-hand side being an approximation for  $\beta_2 \ll 1$ .

## 2.2. RF Power and Field Level Calibration

The RF power ( $P_f$ ,  $P_r$ ,  $P_t$ ) generally cannot be measured directly. Hence RF calibrations are needed to account for the effect of directional couplers, cable attenuation, and other features of the RF system. This allows us to convert from the “signal” power values to the “actual” power values at the input and pickup ports of the cavity. In this report, it is assumed that these calibrations have been done, so that  $P_f$ ,  $P_r$ , and  $P_t$  are actual values. More in-depth discussions of RF calibrations can be found elsewhere, for example Ref. [13].

CW measurements alone are not generally sufficient to calculate all of the derived quantities of interest. We can obtain additional information by doing a “field level calibration” at low power. For SRF cavities, this is typically done with amplitude modulation. An overview of modulated measurement analysis is provided in [Appendix A](#), considering both the traditional case of weak input coupling and the general case of arbitrary pickup coupling. Both  $Q_{ext,1}$  and  $Q_{ext,2}$  can be calculated from modulated measurements, along with  $U$  and  $Q_0$ . For NRF cavities, it is more practical to sweep the frequency rather than modulate the amplitude; an equivalent field level calibration can be done in the frequency domain.

A numerical calculation of the field pattern is needed to establish the relationship between the stored energy and the fields for the mode of interest. This may be done using 2D codes such as SUPERFISH [14, 15] or SuperLANS [16], or 3D codes such

as CST Microwave Studio [17] or Omega3P [18]. The accelerating gradient  $E_a$  is proportional to the square root of the stored energy:

$$E_a \propto \sqrt{U}. \quad (10)$$

The peak surface electric field and peak surface magnetic field are proportional to the square root of  $U$  as well. These and other derived quantities such as the accelerating voltage may be calculated from  $U$  using the output of the numerical calculation.

## 3. CW Analysis

If  $Q_{ext,1}$  and  $Q_{ext,2}$  are known (generally from a low-power field calibration, per [Section 2.2](#)), the CW measurements provide more information than is needed, such that there is more than one way to calculate the stored energy, field, and  $Q_0$ . In principle, the different methods should give the same result. In practice, the answers may be different due to systematic errors, as described above.

### 3.1. Direct Method Using $P_f - P_r - P_t$

The dissipated power  $P_d$  is calculated by subtraction,

$$P_d = P_f - P_r - P_t. \quad (11)$$

The stored energy is related to the transmitted power via [Equation \(2\)](#). Knowing  $P_t$ ,  $Q_{ext,2}$ , and  $f_0$ ,  $U$  may be calculated by rewriting [Equation \(2\)](#) as

$$U = P_t \frac{Q_{ext,2}}{\omega_0}. \quad (12)$$

With  $f_0$ ,  $P_d$ , and  $U$  known,  $Q_0$  may be calculated directly via [Equation \(1\)](#). In terms of measured RF power values, the intrinsic  $Q$  is

$$Q_0 = Q_{ext,2} \left( \frac{P_t}{P_f - P_r - P_t} \right). \quad (13)$$

In terms of measured S-parameters, we have

$$Q_0 = Q_{ext,2} \left( \frac{|S_{21}|^2}{1 - |S_{11}|^2 - |S_{21}|^2} \right). \quad (14)$$

The field may be calculated from  $U$  via [Equation \(10\)](#) with the appropriate scaling coefficient.

Advantages of the direct method include (i) it is straightforward to understand and use; (ii) knowledge of  $Q_{ext,1}$  is not needed. An additional advantage is that the formulae derived above are valid for arbitrary pickup coupler strength.

Disadvantages of the direct method include (i) it makes use of  $P_r$ , which may have significant systematic error associated with it; (ii) it relies on the difference between  $P_f$  and  $P_r$ ; when the input coupling factor is not close to unity,  $P_f - P_r$  is a small number that is the difference of 2 large numbers, which therefore tends to magnify systematic errors.

### 3.2. Indirect Method Using $P_t/P_f$ : Brute Force Derivation

In the previous section, we used 3 equations, namely [Equation \(11\)](#), [Equation \(12\)](#), and [Equation \(1\)](#), to solve for 3 unknowns, namely  $P_d$ ,  $U$ , and  $Q_0$ . We would now like to derive an expression for  $Q_0$  which does not make use of  $P_r$ . This will require an additional equation. We begin with [Equation \(11\)](#), re-writing it in terms of the scattering parameters defined via [Equation \(6\)](#) and [Equation \(7\)](#) to obtain

$$\frac{P_d}{P_f} = 1 - |S_{11}|^2 - |S_{21}|^2. \quad (15)$$

Our additional equation relates the input coupling factor  $\beta_1$  to the ratio  $P_r/P_f$  via [2, Section 8.3]:

$$\beta_1 \approx \frac{1 \pm \sqrt{P_r/P_f}}{1 \mp \sqrt{P_r/P_f}}. \quad (16)$$

In the “ $\pm$ ” and “ $\mp$ ” operators, the upper sign applies for the over-coupled case; the lower sign applies for the under-coupled case. The above equation is an approximation valid if  $\beta_2 \ll 1$ . In terms of  $S$ -parameters, we can write

$$\beta_1 \approx \frac{1 \pm |S_{11}|}{1 \mp |S_{11}|}. \quad (17)$$

Solving for  $|S_{11}|^2$ , we obtain

$$|S_{11}|^2 \approx \left( \frac{1 - \beta_1}{1 + \beta_1} \right)^2. \quad (18)$$

Substituting this expression into [Equation \(15\)](#) and simplifying gives

$$\frac{P_d}{P_f} \approx \frac{4\beta_1}{(1 + \beta_1)^2} - |S_{21}|^2. \quad (19)$$

Since  $\beta_1$  and  $P_d$  are both unknown, we need to eliminate  $P_d$ . Using [Equation \(5\)](#) and [Equation \(7\)](#), we can write  $P_d$  in terms of  $P_f$ ,  $\beta_2$ , and  $|S_{21}|$ :

$$\frac{P_d}{P_f} \approx \frac{|S_{21}|^2}{\beta_2}. \quad (20)$$

Substituting this into [Equation \(19\)](#) gives

$$\frac{|S_{21}|^2}{\beta_2} \approx \frac{4\beta_1}{(1 + \beta_1)^2} - |S_{21}|^2. \quad (21)$$

Let us define a normalized scattering parameter:

$$R_{21} \equiv S_{21} \sqrt{\frac{\beta_1}{\beta_2}} = S_{21} \sqrt{\frac{Q_{ext,2}}{Q_{ext,1}}}, \quad (22)$$

so that, after multiplying by  $\beta_1$  [Equation \(21\)](#) becomes,

$$|R_{21}|^2 \approx \frac{4\beta_1^2}{(1 + \beta_1)^2} - \beta_2 |R_{21}|^2, \quad (23)$$

which can be rearranged to give

$$|R_{21}| \sqrt{1 + \beta_2} \approx \frac{2\beta_1}{1 + \beta_1}. \quad (24)$$

If  $\beta_2 \ll 1$  (i.e. weakly-coupled pickup antenna, as assumed above), then

$$|R_{21}| \approx \frac{2\beta_1}{1 + \beta_1}. \quad (25)$$

Solving for  $\beta_1$ , we obtain

$$\beta_1 \approx \frac{1}{\frac{2}{|R_{21}|} - 1} = \frac{|R_{21}|}{2 - |R_{21}|}. \quad (26)$$

Using [Equation \(3\)](#), we can obtain an expression for  $Q_0$ ,

$$Q_0 \approx \frac{Q_{ext,1}}{\frac{2}{|R_{21}|} - 1} = \left( \frac{|R_{21}|}{2 - |R_{21}|} \right) Q_{ext,1}. \quad (27)$$

Substituting [Equation \(22\)](#) and [Equation \(7\)](#) into the last expression results in an explicit expression for  $Q_0$  in terms of measured powers and coupling strengths,

$$Q_0 \approx \frac{Q_{ext,1}}{2 \sqrt{\frac{Q_{ext,1}}{Q_{ext,2}} \cdot \frac{P_f}{P_t}} - 1}. \quad (28)$$

### 3.3. Indirect Method Using $P_t/P_f$ : Emitted Wave Derivation

In Chapter 8 of Ref. [2], the cavity behavior for cases other than the steady-state case are considered. If the drive power is switched off ( $P_f \rightarrow 0$  at time  $t = 0$ ), one can consider an “emitted power” ( $P_e$ ) which is the instantaneous value of  $P_r$  after  $P_f$  becomes zero. This quantity is related to the coupling strength via [2, Section 8.2.1]

$$Q_{ext,1} = \frac{\omega_0 U}{P_e}. \quad (29)$$

In this case,  $U$  is the value of the stored energy at  $t = 0$ ; the stored energy will then decrease exponentially with time.

The input coupling factor can be expressed in terms of  $P_e$  via [2, Section 8.3.1]

$$\beta_1 \approx \frac{1}{2 \sqrt{\frac{P_f}{P_e}} - 1}. \quad (30)$$

The equation above is again an approximation valid if  $\beta_2 \ll 1$ . We cannot obtain  $P_e$  in a CW measurement. However, using [Equation \(2\)](#) and [Equation \(29\)](#), we can express  $P_e$  in terms of  $P_t$ :

$$P_e = \frac{Q_{ext,2}}{Q_{ext,1}} P_t. \quad (31)$$

We can now substitute [Equation \(31\)](#) into [Equation \(30\)](#) to obtain

$$\beta_1 \approx \frac{1}{2 \sqrt{\frac{Q_{ext,1}}{Q_{ext,2}} \frac{P_f}{P_t}} - 1}. \quad (32)$$

The above equation can be easily seen to be equivalent to [Equation \(28\)](#). Thus, consideration of the emitted power allows us to derive the same results as obtained in the previous section, but using fewer steps.

The present approach provides additional insight if we return to the definition of  $|R_{21}|$  from [Equation \(22\)](#) and use [Equation \(7\)](#) and [Equation \(31\)](#) to express  $|R_{21}|$  in terms of  $P_f$  and  $P_e$ :

$$|R_{21}| = \sqrt{\frac{P_e}{P_f}}. \quad (33)$$

Thus the normalized scattering parameter relates the emitted wave to the forward wave in the same way as  $|S_{21}|$  relates the transmitted wave to the forward wave.

The emitted power can be measured directly by modulation of the drive amplitude. However, mismatches in the input line may produce systematic errors in the  $P_e$  measurement, and the measurement requires more specialized equipment (such as a spectrum analyzer or oscilloscope and RF diode) and hence may require additional calibration steps (as well as attention to the time resolution of the measurement). In effect, this analysis of the CW measurements makes  $P_t$  a proxy for  $P_e$ .

#### 3.4. Indirect Method: Additional Formulae, Comments

Using [Equation \(1\)](#) and [Equation \(2\)](#), we can eliminate  $Q_0$  from [Equation \(28\)](#) and express  $P_d$  explicitly in terms of  $P_f$ ,  $P_t$ , and the coupling strengths:

$$P_d \approx P_t \frac{Q_{ext,2}}{Q_{ext,1}} \left( 2 \sqrt{\frac{Q_{ext,1}}{Q_{ext,2}} \cdot \frac{P_f}{P_t}} - 1 \right). \quad (34)$$

As expected, we no longer need  $P_r$  to calculate  $Q_0$  and  $P_d$ , but we now need  $Q_{ext,1}$ . For an alternative expression, using [Equation \(22\)](#) and [Equation \(7\)](#), we can express  $P_d$  in terms of  $|R_{21}|$  and  $P_f$ :

$$P_d \approx |R_{21}| (2 - |R_{21}|) P_f. \quad (35)$$

Advantages of the indirect method include (i) it does not use  $P_r$ , so systematic errors in the  $P_r$  measurement are avoided; (ii) it does not rely on the calculation of  $P_f - P_r$ , the calculation of which may be problematic when not close to unity coupling.

Disadvantages of the indirect method include (i) the derivation of the formula is more complicated and its application may be less intuitive; (ii) it requires both  $Q_{ext,1}$  and  $Q_{ext,2}$ ; (iii) the formula may not work well when the cavity is strongly over-coupled. We will return to the latter point in [Section 5](#).

An additional disadvantage of the indirect method as derived in this section is that we assume a weak pickup coupler. The case of arbitrary pickup coupler strength is discussed in [Appendix B.2](#).

### 4. Graphical Assessment Method: Derivation

The graphical method to assess measurement consistency described in this report is used both for “real time” assessments during SRF cavity cold tests at MSU and for consistency evaluation in the final analysis of cold tests.

[Equation \(17\)](#) gives  $\beta_1$  in terms of  $|S_{11}|$ ; [Equation \(26\)](#) gives  $\beta_1$  in terms of  $|R_{21}|$ . Eliminating  $\beta_1$  gives us

$$\frac{1 \pm |S_{11}|}{1 \mp |S_{11}|} = \frac{|R_{21}|}{2 - |R_{21}|}. \quad (36)$$

Solving for  $|R_{21}|$  gives

$$|R_{21}| = 1 \pm |S_{11}|. \quad (37)$$

Since we must always have  $0 \leq |S_{11}| \leq 1$ , [Equation \(37\)](#) tells us that the values of  $|S_{11}|$  and  $|R_{21}|$  should always be on one of the two equal sides of an isosceles triangle, as shown in [Figure 1](#). We refer to it as the “Duality Triangle.” When doing CW measurements,  $|S_{11}|$  and  $|R_{21}|$  can be calculated from  $Q_{ext,1}$ ,  $Q_{ext,2}$ ,  $P_f$ ,  $P_r$ , and  $P_t$ . The proximity of these values to the Duality Triangle then provides an indication of the self-consistency of the measured values.

As discussed, in [Section 3.3](#), the indirect analysis effectively uses the transmitted wave of the pickup coupler as a proxy for the emitted wave of the input coupler, since the latter cannot be measured in CW; the vertical axis of the Duality Triangle can

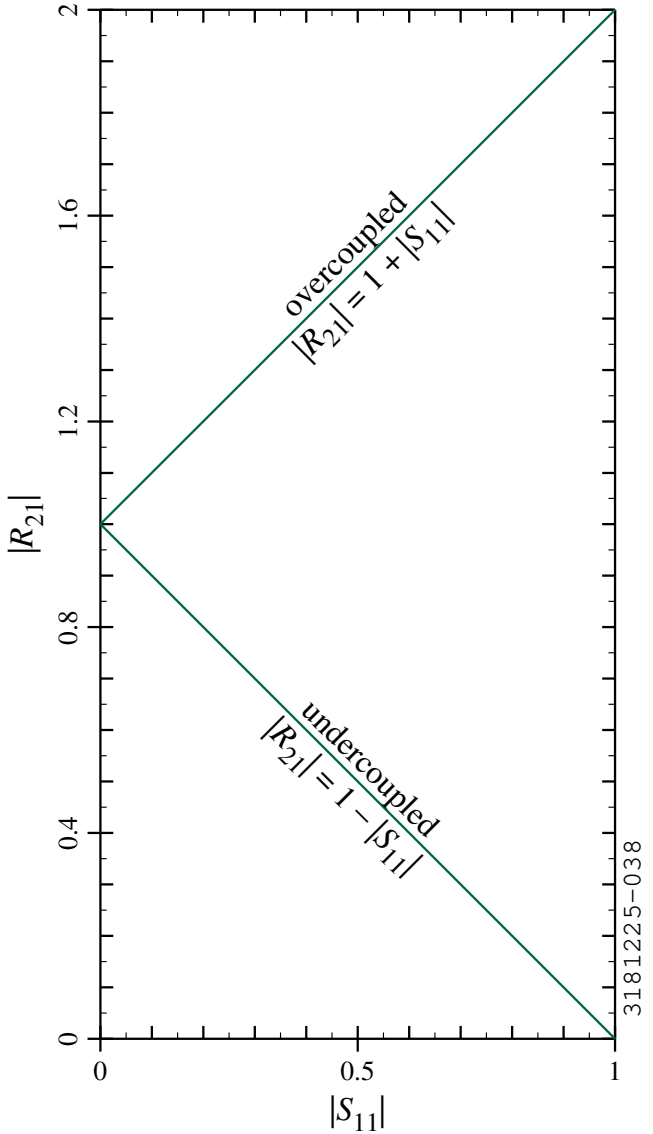


**Figure 1.** The “Duality Triangle.” In CW measurements, the calculated values of  $|S_{11}|$  and  $|R_{21}|$  should fall on the lower or upper green line segments.

hence be thought of as representing the scattering parameter for the emitted wave, as inferred from the transmitted wave. If we use [Equation \(33\)](#) and [Equation \(6\)](#) to rewrite [Equation \(37\)](#) in terms of  $P_f$ ,  $P_r$ , and  $P_e$ , we obtain

$$\sqrt{\frac{P_e}{P_f}} = 1 \pm \sqrt{\frac{P_r}{P_f}}. \quad (38)$$

As a consistency check, we note that the above equation is equivalent to Equation (8.46) in Ref. [2].

As discussed previously, the lower sign corresponds to the undercoupled case, so that, from [Equation \(37\)](#),  $|R_{21}|$  is less than 1; for the upper sign, the overcoupled case,  $|R_{21}|$  is greater than 1. Hence the lower side of the Duality Triangle corresponds to the undercoupled case and the upper side corresponds to the overcoupled case, as indicated in [Figure 1](#).

Although we have assumed a weak pickup coupler for this derivation, [Appendix B.3](#) shows that the results presented in this section are valid for arbitrary pickup coupling strength, provided  $Q_{ext,1}$  and  $Q_{ext,2}$  are calculated properly (per [Appendix A.3](#)). Thus, applications of the Duality Triangle are not limited to the case of  $\beta_2 \ll 1$ , and we replaced the “approximately equal to” signs with “equal to” signs in the equations above.

Though the Duality Triangle provides a way to check the self-consistency of the measured values of  $P_f$ ,  $P_r$ , and  $P_t$  (used to obtain  $|S_{11}|$  and  $|S_{21}|$ ) with the calculated values of  $Q_{ext,1}$  and  $Q_{ext,2}$  (used to calculate  $|R_{21}|$  from  $|S_{21}|$ ), consistency with the Duality Triangle does not guarantee that the results are valid. One counterexample is a scenario in which the calculated values of both  $Q_{ext,1}$  and  $Q_{ext,2}$  are too large by a factor of 2. In this case,  $|R_{21}|$  is unaffected, and the Duality Triangle does not show a discrepancy. Hence, as always, the cavity test analysis team should proceed with care.

## 5. Graphical Assessment Method: Vertices and Limiting Cases

### 5.1. Weak Input Coupling

From [Equation \(25\)](#), if  $\beta_1 \ll 1$ ,  $|R_{21}| \approx 2\beta_1$ ; hence  $|R_{21}|$  approaches zero for  $\beta_1 \rightarrow 0$ . Thus the lower vertex of the Duality Triangle ( $|S_{11}| = 1$ ,  $|R_{21}| = 0$ ) corresponds to the weak input coupling limit,  $\beta_1 \ll 1$ , or, equivalently,  $Q_{ext,1} \gg Q_0$ . In the vicinity of the weak coupling limit, the  $Q_0$  value from the direct method may have excessive error due to  $P_f - P_r$  being a small difference between 2 large numbers; the  $Q_0$  value from the indirect method may be less prone to systematic error if the coupling strengths are known with reasonable accuracy. In this case,  $P_e$  is small compared to  $P_f$  and  $P_d$  and  $P_r$  is approximately equal to  $P_f$ .

Explicit expressions from the indirect method in the weak input coupling limit are

$$Q_0 \approx \frac{|R_{21}|}{2} = \frac{1}{2} \sqrt{\frac{P_t}{P_f}} \sqrt{Q_{ext,1} Q_{ext,2}}, \quad (39)$$

$$P_d \approx 2|R_{21}|P_f = 2\sqrt{P_t P_f} \sqrt{\frac{Q_{ext,2}}{Q_{ext,1}}}. \quad (40)$$

A variant of [Equation \(39\)](#) may be familiar to some readers in the context of room temperature measurements on SRF cavities.

### 5.2. Unity Input Coupling

Setting  $\beta_1 = 1$  in [Equation \(25\)](#) gives  $|R_{21}| = 1$ . Thus the middle vertex of the Duality Triangle ( $|S_{11}| = 0$ ,  $|R_{21}| = 1$ ) corresponds to the unity input coupling case,  $\beta_1 = 1$  and  $Q_{ext,1} = Q_0$ . In the vicinity of unity coupling, one can hope that both the direct method and the indirect method will produce reasonable results. Near unity coupling,  $P_e$  is approximately equal to  $P_f$  and  $P_r$  is approximately zero.

### 5.3. Strong Input Coupling

For large values of  $\beta_1$ , [Equation \(25\)](#) shows that  $|R_{21}|$  approaches 2. Thus, the upper vertex of the Duality Triangle ( $|S_{11}| = 1$ ,  $|R_{21}| = 2$ ) corresponds to the strong input coupling limit,  $\beta_1 \gg 1$  and  $Q_{ext,1} \ll Q_0$ . In the vicinity of the strong coupling limit, the  $Q_0$  value from the direct method may have excessive error due to  $P_f - P_r$  being a small difference between 2 large numbers; the  $Q_0$  value from the indirect method may be problematic as well, because the denominator in [Equation \(27\)](#) approaches zero in the limit in which  $|R_{21}|$  approaches 2. The measured power ratios are mainly determined by the couplers and are not sensitive to the cavity  $Q_0$ . In this case,  $P_r$  is again approximately equal to  $P_f$  and  $P_e$  is approximately equal to  $4P_f$ . The latter result may be familiar to readers who use pulsed systems.

## 6. Detuning

So far, we have assumed that the cavity is driven on resonance. In this section, we will consider the more general case in which the drive frequency is not necessarily equal to the resonant frequency.

### 6.1. Graphical Assessment Method: Detuning Predictions

Analyses of cavity behavior as a function of drive frequency can be found in the literature, for example in Chapter 8 of Ref. [2]. Useful formulae for the S-parameters as a function of the drive angular frequency  $\omega = 2\pi f$  are

$$S_{11}(\omega) = \frac{\beta_1 - 1 - iQ_0 \left( \frac{\omega}{\omega_0} - \frac{\omega_0}{\omega} \right)}{\beta_1 + 1 + iQ_0 \left( \frac{\omega}{\omega_0} - \frac{\omega_0}{\omega} \right)} \quad (41)$$

and

$$|S_{21}(\omega)| = \sqrt{\frac{Q_{ext,1}}{Q_{ext,2}}} \frac{2\beta_1}{\sqrt{(\beta_1 + 1)^2 + \left[ Q_0 \left( \frac{\omega}{\omega_0} - \frac{\omega_0}{\omega} \right) \right]^2}}, \quad (42)$$

where, again,  $\omega_0$  is the resonant angular frequency. The above are obtained from Eq. (8.42) and Eq. (8.30) in Ref. [2]. Using the definition of  $|R_{21}|$ , we can write

$$|R_{21}(\omega)| = \frac{2\beta_1}{\sqrt{(\beta_1 + 1)^2 + \left[ Q_0 \left( \frac{\omega}{\omega_0} - \frac{\omega_0}{\omega} \right) \right]^2}}. \quad (43)$$

The basic response of the cavity according to the above equations is illustrated in [Figure 2](#), which shows  $|S_{11}|$  and  $|R_{21}|$  as a function of the relative frequency ( $f$  = drive frequency,  $f_0$  = resonant frequency) for  $Q_0 = 10^3$  and  $\beta_1$  values ranging from 0.125 to 8. The patterns seen in [Figure 2](#) are likely familiar to most readers: there is a minimum in  $|S_{11}|$  and a maximum in  $|R_{21}|$  on resonance;  $|S_{11}|$  approaches 1 and  $|R_{21}|$  approaches 0 for large detuning;  $|S_{11}|$  reaches 0 on resonance when  $\beta_1 = 1$ ; the bandwidth is smaller for low  $\beta_1$  values and larger for high  $\beta_1$  values. The maximum value of  $|R_{21}|$  approaches 2 for large  $\beta_1$ , consistent with [Section 5.3](#).

[Figure 3a](#) shows a polar plot of  $S_{11}$  as a function of drive frequency for different values of  $\beta_1$ , which will likely be familiar to most reader as well. As the drive frequency varies,  $S_{11}$  traces out a circle in the complex plane. The path traced out in the complex plane is dependent on  $\beta_1$ , but not on  $Q_0$ . The circle encloses the origin if  $\beta_1 > 1$  but not if  $\beta_1 < 1$ .

[Figure 3b](#) shows the corresponding curves traced out in the  $|S_{11}|-|R_{21}|$  plane as the drive frequency varies, with the Duality

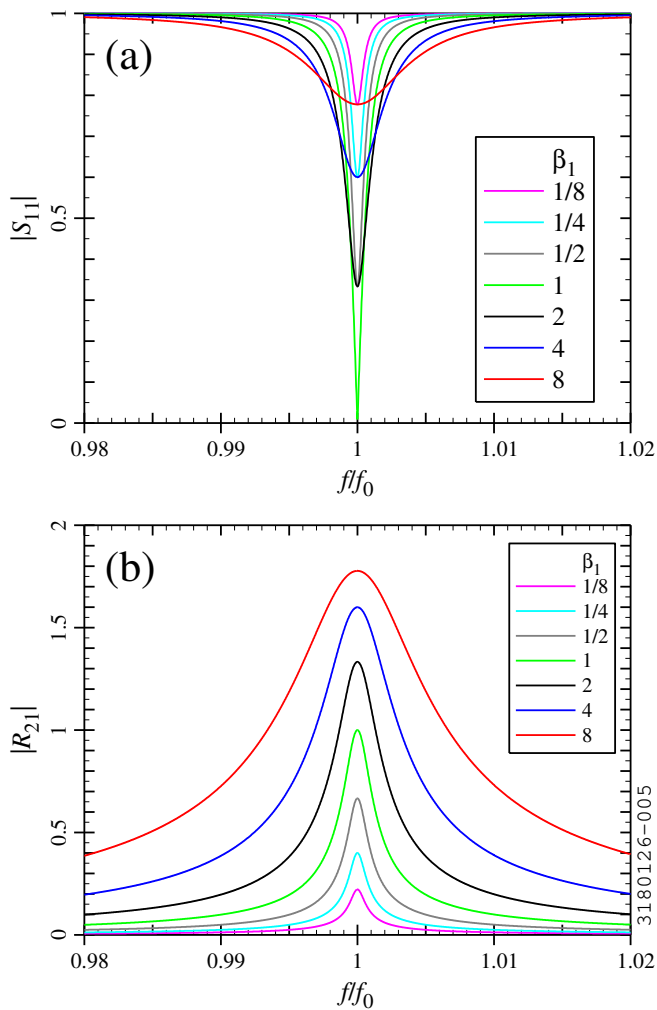


**Figure 2.** Calculated scattering parameters as a function of normalized drive frequency for a cavity with  $Q_0 = 10^3$ : (a)  $|S_{11}|$  and (b)  $|R_{21}|$ .

Triangle shown in dark green. Again, the path is dependent on  $\beta_1$ , but not on  $Q_0$ . On resonance, the values lie on the Duality Triangle. Off resonance points lie inside the Duality Triangle. This is consistent with [Figure 2a](#), in which the minimum in  $|S_{11}|$  occurs on resonance, and  $|S_{11}|$  increases when we go off resonance. As we go further and further off resonance, we approach a “fully detuned” limit,  $|S_{11}| = 1$ ,  $|R_{21}| = 0$ , which is the same as the weak coupling limit.

[Figure 3c](#) shows a polar plot of  $S_{11}$  as a function of  $\beta_1$  for for different values of relative drive frequency offset. The on-resonance case is a horizontal line through the origin (green). The off-resonance cases produce straight lines that do not intersect the origin. Each curve had a different value of  $(f - f_0)/\Delta f$ ; normalizing to the loaded bandwidth  $\Delta f$  should produces curves similar to the those obtained by driving the cavity in phase-lock mode with a constant offset in the loop phase. (The results which be somewhat different for a an open-loop scenario with the cavity drive with a constant offset in the drive frequency.)

[Figure 3d](#) shows the corresponding curves traced out in the  $|S_{11}|-|R_{21}|$  plane as  $\beta_1$  varies, with the Duality Triangle shown in dark green. On resonance, the values lie on the Duality Triangle (light green). Off-resonance curves lie inside the Duality Triangle, as expected. Positive and negative relative frequency offsets lie on the same curve in the  $|S_{11}|-|R_{21}|$  plane. Once again, the paths traced out in the complex plane and in the  $|S_{11}|-|R_{21}|$  plane are independent of  $Q_0$ .

## 6.2. Graphical Assessment Method: Detuning Measurements

In the case of CW measurements on SRF cavities, it is impractical to sweep the drive frequency, as the bandwidth is typically comparable to the resonant frequency fluctuations from microphonics. However, in phase lock-loop mode, a similar effect can be achieved by varying the loop phase. [Figure 4](#) shows some examples of such measurements on FRIB HWRs. [Figure 4a](#) and [Figure 4c](#) show polar plots for different  $\beta_1$  values. In these measurements, we set the forward power to establish a low field in the cavity ( $E_a$  between 1 and 2 MV/m typically) and kept the forward power constant which varying the loop phase, so that the cavity field decreased as the loop phase offset increased. The results are consistent with expectations, though the curves are rotated by an arbitrary phase offset relative to the predictions of [Figure 3a](#) (this is as expected, as the measured phases are not corrected for the phase advance along the transmission lines between the couplers and the phase measurement planes); In addition, due to systematic errors,  $|S_{11}|$  is slightly larger than 1 for some cases.

[Figure 4b](#) and [Figure 4d](#) show the corresponding results in the  $|S_{11}|-|R_{21}|$  plane. Again, the results are consistent with expectations, although  $|S_{11}|$  is again slightly larger than 1 for some cases. As predicted, the values lie on the Duality Triangle when on resonance; the values lie inside the Triangle when off resonance; and the values approach the lower right vertex for large detuning.

In [Figure 4a](#) and [Figure 4b](#), the coupler position was fixed and bath temperature was adjusted to change from undercou-

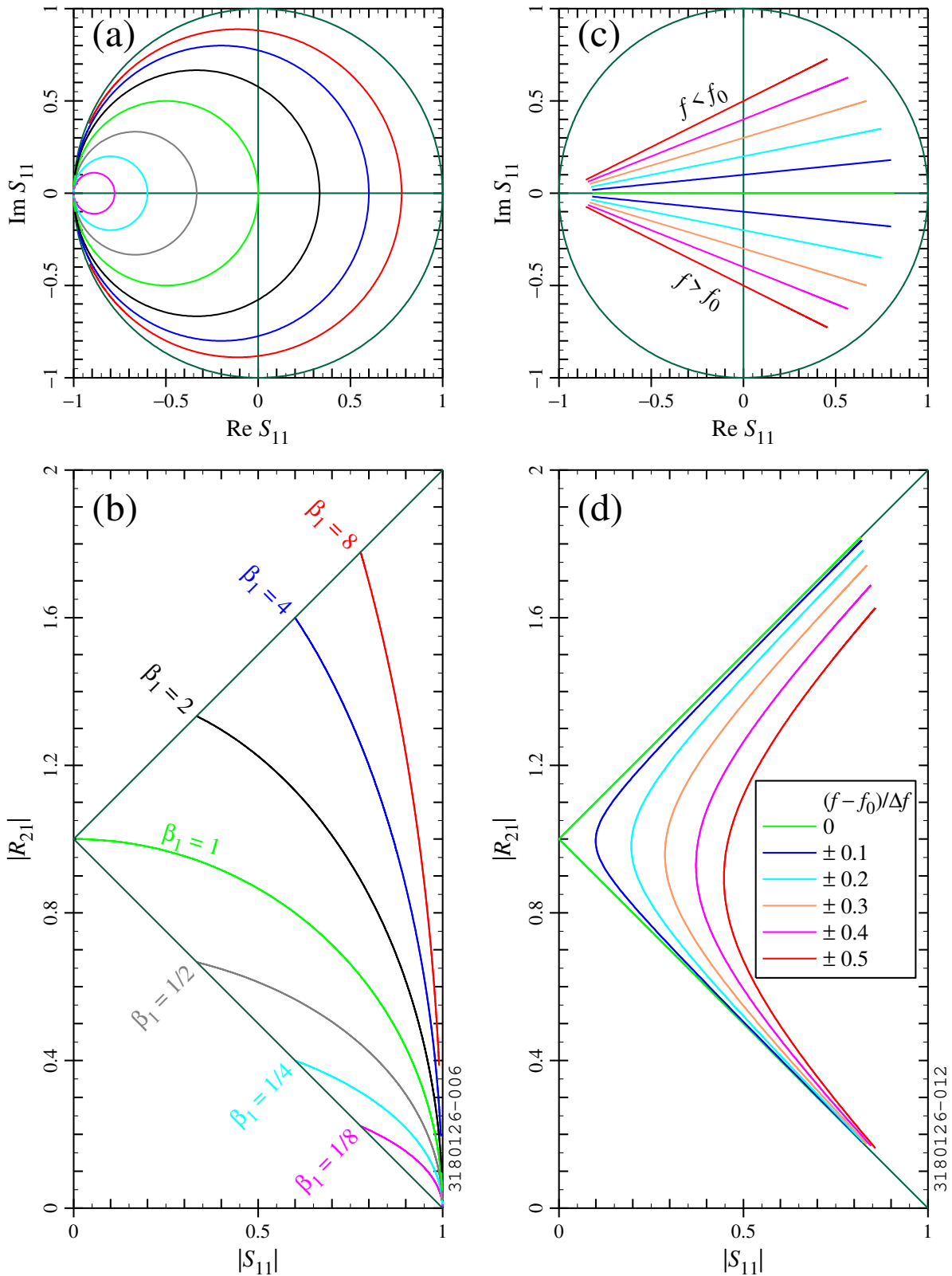


**Figure 3.** (a) Polar plot of  $S_{11}$  and (b) curves traced out in the  $|S_{11}|-|R_{21}|$  plane as a function of drive frequency. (c) Polar plot of  $S_{11}$  and (d) curves traces out in the  $|S_{11}|-|R_{21}|$  plane as a function of  $\beta_1$ .

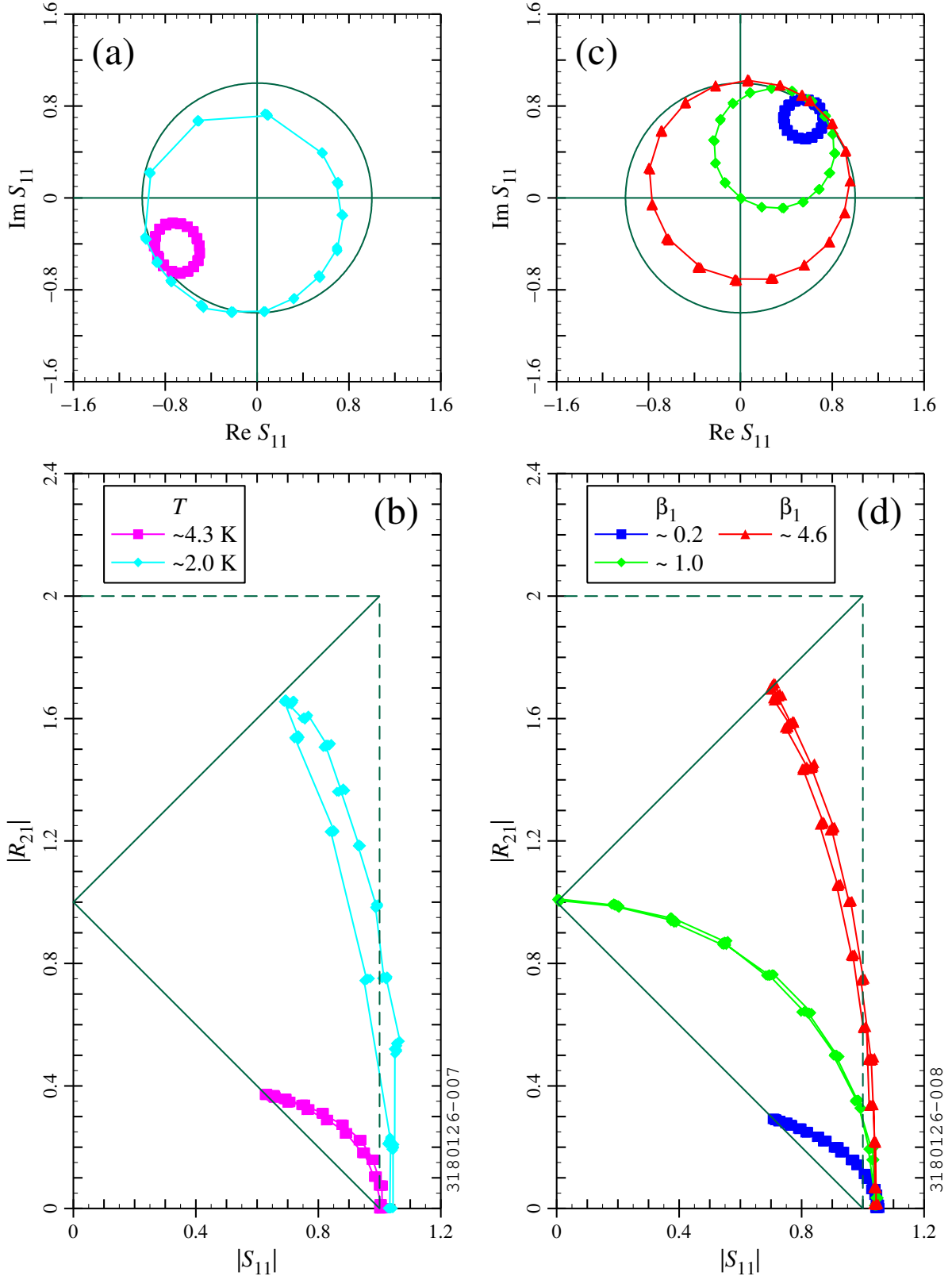


**Figure 4.** CW measurements on FRIB HWRs as a function of loop phase: (a) polar plot of  $S_{11}$  and (b)  $|S_{11}|$  vs  $|R_{21}|$  at 2 different bath temperatures (S53-028, December 2017); (c) polar plot of  $S_{11}$  and (d)  $|S_{11}|$  vs  $|R_{21}|$  for 3 different coupler positions (S53-121, October 2018).

pled to overcoupled. The same values of  $Q_{ext,1}$  and  $Q_{ext,2}$  are used in the data analysis (obtained via modulated measurements).

In [Figure 4c](#) and [Figure 4d](#), the bath temperature was fixed (4.3 K), but a variable coupler was used, allowing us to achieve different  $\beta_1$  values via coupler position adjustment. The values of  $Q_{ext,1}$  were not measured for every coupler position, so estimated  $Q_{ext,1}$  values were used, based on the measured  $S_{11}$  values, the measured  $Q_0$  values, and consistency of the Duality Triangle.

Per [Figure 3b](#), we expect negative and positive detuning to take us along the same path in the plane, but the measurements of [Figure 4b](#) and [Figure 4d](#) show some discrepancies between positive and negative detuning, as seen by the double-valued curves. This tends to be more pronounced in the overcoupled cases. The cause may again be systematic errors in the measured values.

### 6.3. Quality Factor Calculation with Detuning: Predictions

Ideally, CW measurements are done with the drive frequency ( $f$ ) equal to the resonant frequency ( $f_0$ ). In practice, there may be some offset between  $f$  and  $f_0$  due to systematic errors, imperfect drive frequency tuning in the open-loop case, or imperfect optimization of the loop phase in the phase-lock case. Hence we cannot always be sure that  $Q_0$  is calculated with  $f$  exactly equal to  $f_0$ .

When using the direct method, the calculated  $Q_0$  depends on  $|S_{11}|^2$  and  $|S_{21}|^2$ . Using [Equation \(14\)](#), [Equation \(41\)](#), and [Equation \(42\)](#), we can see that, at least in the case of a weak pickup coupler, the calculated  $Q_0$  is in principle the same for  $f \neq f_0$  and  $f = f_0$ . In this case, both  $|S_{21}|^2$  and  $1 - |S_{11}|^2$  depend on the frequency, but their ratio does not.

This is in contrast to the indirect method, in which  $Q_0$  depends on  $|R_{21}|$ , per [Equation \(27\)](#). As  $|R_{21}|$  changes with frequency, the calculated  $Q_0$  follows suit. These findings are illustrated in [Figure 5a](#): the calculated  $Q_0$  is independent of detuning when we use the direct method (black), but decreases with detuning when we use the indirect method (light colors). The calculated indirect  $Q_0$  decreases more rapidly with detuning when undercoupled (cyan) and decreases more slowly with detuning when overcoupled (magenta). These trends are qualitatively consistent with the loaded bandwidth being smaller when undercoupled and larger when overcoupled.

[Figure 5b](#) shows the same results, but with the frequency normalized to the loaded bandwidth  $\Delta f$  defined via [Equation \(9\)](#). This normalization should be on par with the case of a loop phase offset in phase-lock mode. With this normalization, the overcoupled case shows greater sensitivity to detuning than the undercoupled case. In other words, with the indirect method, detuning by the same fraction of the bandwidth or by the same loop phase offset should produce a bigger  $Q_0$  error with stronger coupling.

### 6.4. Quality Factor Calculation with Detuning: Measurements

We can calculate  $Q_0$  as a function of detuning for the measurements as a function of loop phase of [Section 6.2](#). [Figure 6](#) shows the corresponding  $Q_0$  calculations for the results shown

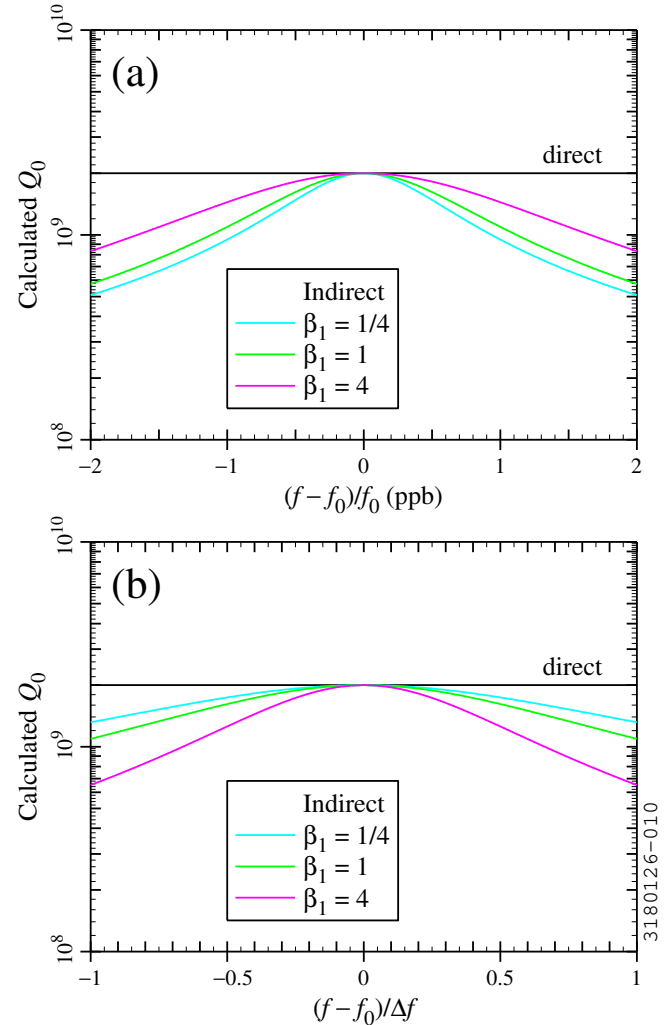


**Figure 5.** Calculated  $Q_0$  values via the indirect method as a function of (a) relative detuning in parts per billion and (b) detuning normalized to the bandwidth  $\Delta f$ , with an actual  $Q_0$  of  $2 \cdot 10^9$ ; black line:  $Q_0$  calculated via the direct method.

in [Figure 4c](#) and [Figure 4d](#) (measurements at 4.3 K, 3 different coupler positions). As described above, the measurements were done at a relatively low accelerating gradient ( $E_a \sim 1.5$  MV/m when on resonance). The direct method (dark colors) shows a small increase in calculated  $Q_0$  for large detuning. This may be explained in part by the decrease in the cavity field with detuning (with the forward power fixed while varying the loop phase), which should produce a slight increase in the measured  $Q_0$  due to “ $Q$ -slope” (an example of the  $Q$ -slope at 4.3 K can be seen in [Figure 9](#) below). We estimate that the  $Q$ -slope should produce an increase in  $Q_0$  of about 10%, which is less than the worst-case differences seen in the direct-calculation  $Q_0$  values. Hence there may be other effects contributing to the apparent  $Q_0$  increase.

The indirect method (light colors) shows more pronounced decreases in the calculated  $Q_0$  values with detuning. As discussed above, adjustment of the loop phase should be analogous to shifting the drive frequency relative to the loaded bandwidth,

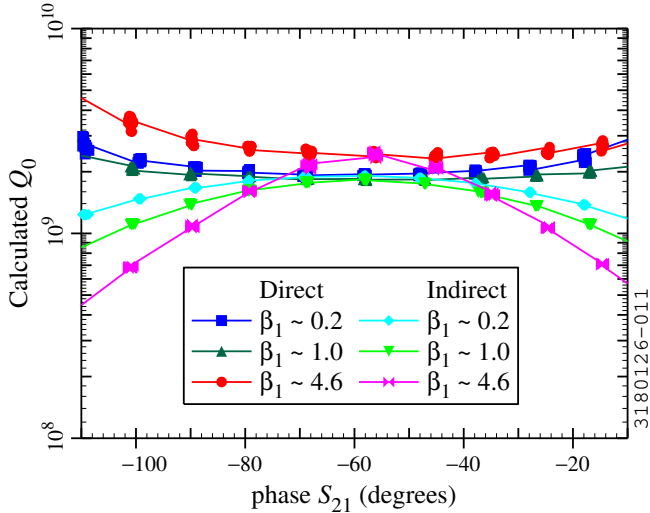


**Figure 6.** Calculated  $Q_0$  values via the direct method (dark colors) and indirect method (light colors) as a function of loop phase based on CW measurements on a FRIB HWR (S53-121, October 2018) at 4.3 K.

so we would expect the behavior to be similar to that seen in Figure 5b. The predictions of Figure 5b and the measurements of Figure 6 are indeed consistent, at least at qualitatively.

Ideally, the calculated  $Q_0$  values on resonance should be the same for the undercoupled, matched, and overcoupled cases. However, Figure 6 shows that the calculated  $Q_0$  is a bit higher for the overcoupled case. This is true for both the direct method (red circles) and the indirect method (magenta bowties). This may be due to systematic errors in the measurements. Though we did not measure  $Q_{ext,1}$  for each coupler position, the consistency between the indirect and direct calculation suggests that the difference in calculated  $Q_0$  is not due to an error in  $Q_{ext,1}$ .

Predictions and measurements show that the indirect method is at a disadvantage relative to the direct method, as the calculated  $Q_0$  is more sensitive to detuning. However, this should not be a problem if the cavity can be driven reasonably close to the resonant frequency. The frequency sensitivity of the indirect method is nevertheless something to keep in mind for scenarios in which the frequency offset is inadvertently high.

## 7. Applications and Examples

All FRIB production cavities were Dewar tested after jacking [8]. In a typical test, CW and modulated measurements are first done at 4.3 K, along with conditioning of multipacting barriers if needed. The cavity is then cooled to 2 K by pumping on the helium bath; low-field CW measurements are usually done during the pump-down to infer the low-field  $Q_0$  as a function of temperature. CW and modulated measurements are repeated at 2 K. The cool-down to 2 K is often paused at 3 K for additional modulated and/or CW measurements. Most of the Dewar tests are done with FRIB low-level RF controllers [19], which allow for both amplitude and phase measurements of the forward, reverse, and transmitted signals. The majority of the tests have been done with fixed RF couplers, though some

tests were done with variable input couplers (allowing us to adjust the coupler position during the cold test). Cold tests for the FRIB energy upgrade are done with an analog RF system without phase measurements.

The Duality Triangle has been found to be useful for real-time feedback during Dewar certification tests. We have used it to trouble-shoot issues with the RF system and check the consistency of field level calibrations.

All FRIB production cryomodules were cold tested prior to installation into the linac tunnel [20]. The Duality Triangle allows for real-time feedback during cryomodule tests. Some examples of Duality Triangle applications for Dewar tests and cryomodule tests will be presented in this section.

### 7.1. Dewar Tests: Real-Time

One application of the Duality Triangle is to detect loop phase errors in phase-lock loop mode. Some examples are included in Figure 7, which shows CW measurements taken on FRIB  $\beta_m = 0.54$  HWRs while pumping on the liquid helium bath to reduce the temperature from 4.3 K to 2 K ( $\beta_m$  = optimum normalized beam speed  $v/c$ ). We expect  $Q_0$  to increase as the temperature increases, such that we should go from undercoupled at 4.3 K to overcoupled at 2 K. In the first data set (green squares), we observe that the measurements of  $S_{11}$  fall along a straight line that intersects the origin (Figure 7a) and the data points fall on the sides of the Duality Triangle (Figure 7b). This is the expected behavior and is consistent with the green curve of Figure 3c and Figure 3d (taking into consideration that  $S_{11}$  has a phase offset, so the on-resonance line is not necessarily horizontal).

For the other data sets (red diamonds, gray and blue triangles), initially the  $S_{11}$  curve does not intersect the origin in Figure 7a (“init” denotes the initial undercoupled measurements); and the data do not intersect the left vertex of the Duality Triangle in Figure 7b. Per Figure 3c and Figure 3d, both of these observations point to the possibility that the loop phase is such that the cavity is driven off resonance (with a lesser offset in the case of the blue triangles and with a greater offset in the case of the red diamonds and gray triangles). Partway through the pump-down, we adjusted the loop phase. As a result, for the upper portion of the Duality Triangle, the data lie closer to the side of the Duality Triangle (Figure 7b), and a portion of the  $S_{11}$  curve can be extrapolated back to intersect the origin (Figure 7a; “fin” denotes the final overcoupled measurements, after phase adjustments).

The need to adjust the loop phase during the pump-down is not unexpected. As seen in Figure 2a, the minimum in  $S_{11}$  is sharper when  $\beta_1$  is close to 1, so the sensitivity to phase errors is more acute when we are near the left vertex of the Duality Triangle. Likewise, per Figure 3d, a given loop phase error produces a bigger discrepancy relative to the Duality Triangle near the left vertex.

We note that, in the case of FRIB cavity tests, loop phase errors can be seen via both the polar  $S_{11}$  plot and the Duality Triangle. On the other hand, for more typical cases in which the RF phases are not measured, a polar  $S_{11}$  plot cannot be used to detect loop phase errors, but the Duality Triangle can be.

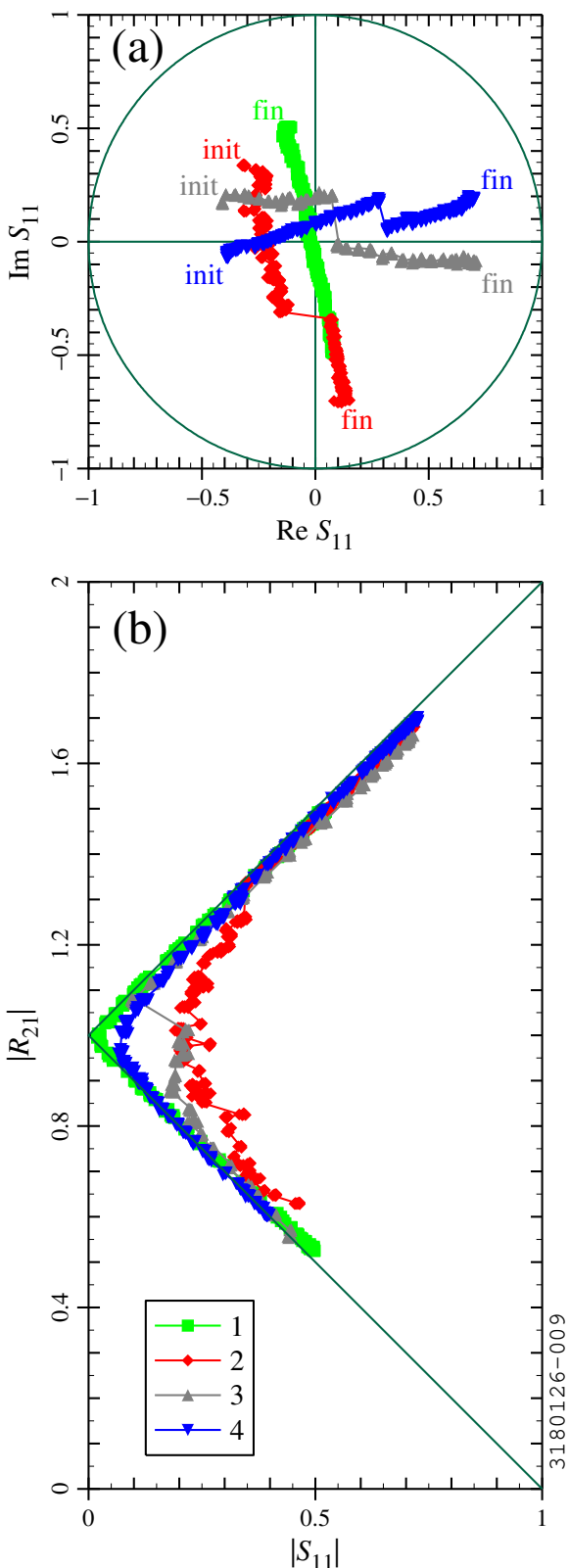


**Figure 7.** CW measurements on FRIB HWRs while pumping from 4.3 K to 2 K: (a) polar plot of  $S_{11}$  and (b)  $|S_{11}|$  vs  $|R_{21}|$  (S53-159 and S53-161, total of 4 tests, May 2023 to Jul 2024).

## 7.2. Dewar Tests: Final Analysis

In the final analysis stage, we have used the Duality Triangle to assess the self-consistency of field level calibrations based on modulated measurements at different temperatures. Ideally, all of the modulated measurements should give the same results for coupling strengths, but we typically observe differences from one measurement to another. As an example, the coupling strengths calculated for a FRIB  $\beta_m = 0.54$  HWR (S53-155, a spare HWR tested in October 2022) from modulated measurements at different temperatures ( $T = \text{bath temperature}$ ) are shown in Table 1. The spread in values is about 10% for both  $Q_{ext,1}$  and  $Q_{ext,2}$ .

CW measurements were done at the same three bath temperatures. The corresponding values of  $|S_{11}|$  and  $|R_{21}|$  from the CW measurements are shown in Figure 8. The measured values (markers) do not fall exactly on the sides of the Duality Triangle (dark green lines). Overall, the coupling strengths obtained at  $\sim 3$  K provide the best consistency (Figure 8b), although there are discrepancies for the undercoupled measurements (the red squares, particularly). The coupling strengths obtained at  $\sim 4.3$  K (Figure 8a) and  $\sim 2.0$  K (Figure 8c) clearly show more overall discrepancy, disagreeing especially in the overcoupled cases (blue triangles, particularly). Note that the modulated measurements at  $\sim 3$  K had the least input coupler mismatch (closest to unity coupling).

During FRIB cavity production, we used the modulated measurement with the best consistency for the final analysis of the CW measurements. In this example, we used the modulated measurements at  $\sim 3$  K. Because the input coupler was approximately matched for typical FRIB cavity Dewar tests, we used the direct method to calculate  $Q_0$  in the final analysis for all FRIB production cavities. The final-analysis values of  $Q_0$  as a function of field for the present example are shown in Figure 9.

For reference, Figure 10 compares the direct and indirect methods to obtain  $Q_0$  from CW measurements at  $\sim 2$  K and compares the results from the modulated measurements at different temperatures. In this example, which is typical of FRIB cavity certification tests, the spread in  $Q_0$  values from one case to another is approximately 25% or less; the differences in  $E_a$  from one case to another are approximately 8% or less.

The present example shows that systematic errors are not negligible for FRIB resonator tests. The Duality Triangle provides a method to assess consistency and try to minimize discrepancies. The discrepancies suggest that a more advanced vector correction method may be beneficial for reduction of sys-

**Table 1.** Calculated coupling strength values from modulated measurements on a  $\beta_m = 0.54$  HWR at different temperatures.

$T$ (K)	$Q_{ext,1}$	$Q_{ext,2}$
$\sim 4.3$	$6.69 \cdot 10^9$	$5.60 \cdot 10^{11}$
$\sim 3.0$	$6.27 \cdot 10^9$	$5.79 \cdot 10^{11}$
$\sim 2.0$	$6.05 \cdot 10^9$	$5.26 \cdot 10^{11}$

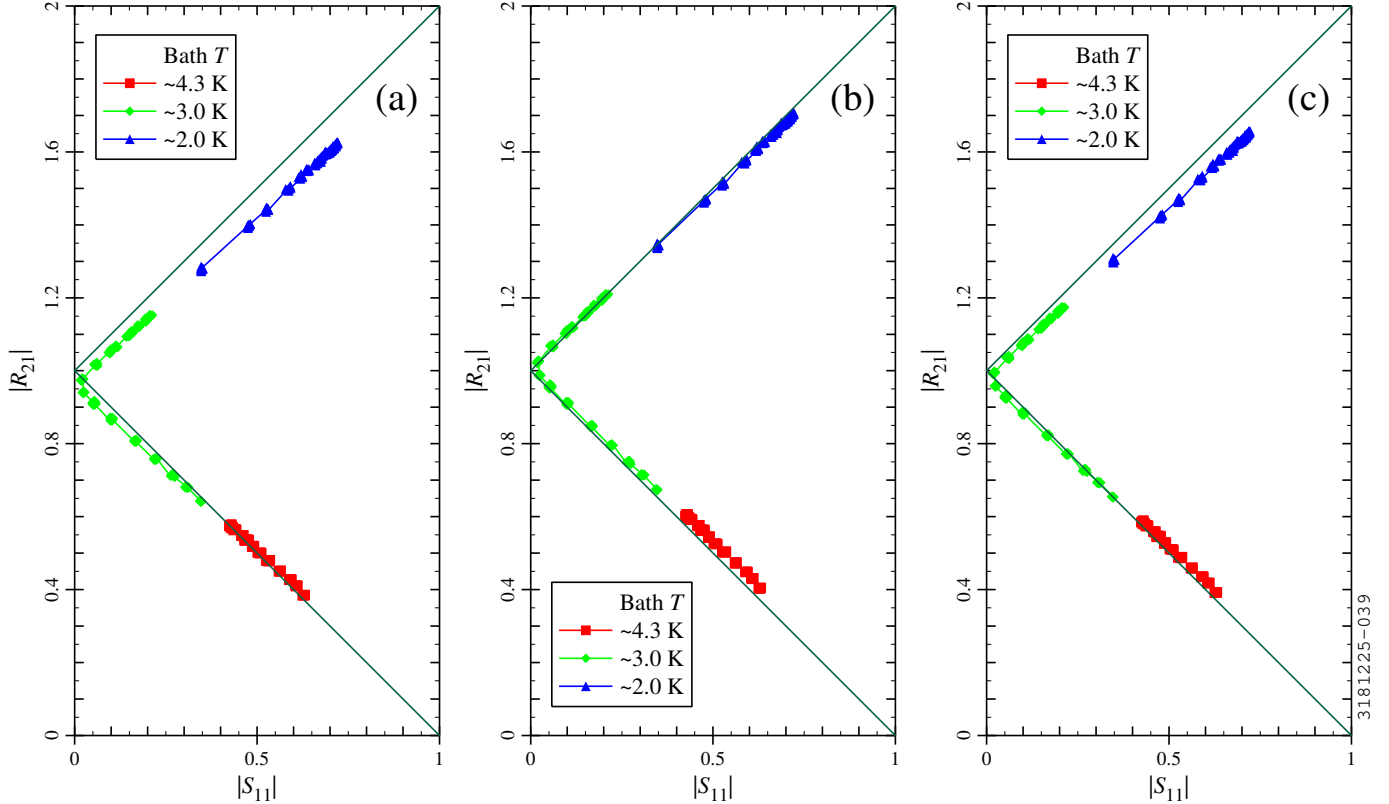


**Figure 8.** Scattering parameters for CW measurements on a  $\beta_m = 0.54$  HWR at three different bath temperatures. The coupling strengths are obtained from modulated measurements at (a)  $\sim 4.3$  K, (b)  $\sim 3.0$  K, and (c)  $\sim 2.0$  K.

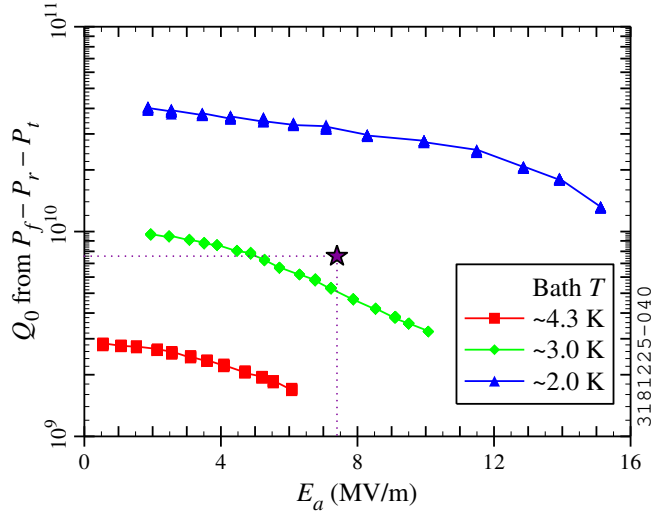


**Figure 9.** Quality factor calculated via the direct method as a function of accelerating gradient for CW measurements on a  $\beta_m = 0.54$  HWR at three different bath temperatures; the coupling strengths are obtained from modulated measurements  $\sim 3.0$  K for all cases. Purple star: design goal for operation at 2 K.

tematic errors, as discussed in [Section 1](#). Although the Duality Triangle helps to recognize discrepancies and minimize their adverse impact, a vector correction method could in principle remove the systematic errors in a more rigorous way and significantly improve the accuracy of the CW measurement results.

### 7.3. Cryomodule Tests

Some examples of “near-real-time” cryomodule test results are shown in [Figure 11](#). As expected, all of the measured values are near the strong coupling limit ( $|S_{11}| = 1, |R_{21}| = 2$ ), as the FPCs are set to be overcoupled for control of amplitude and phase in the presence of microphonics and beam loading.

[Figure 11a](#) shows results for a  $\beta_m = 0.086$  cryomodule containing 8 QWRs (SCM813, tested in July 2023). Field emission X-rays were observed for some of the the cavities at high field. There is significant scatter between cavities, such that sometimes  $|S_{11}| > 1$  and  $|R_{21}| > 2$ ; this confirms that the systematic errors in the measured values of  $P_f$ ,  $P_r$ , and  $P_t$  are significant enough to make it difficult to infer  $P_d$  and  $Q_0$ .

[Figure 11b](#) shows results for a  $\beta_m = 0.29$  HWR cryomodule containing 6 HWRs (SCM207, tested in early February 2019). No field emission was observed, but some of the CW measurements were taken while conditioning the high multipacting barrier. The results are more consistent with the Duality Triangle, but some of the values still have  $|S_{11}| > 1$  and  $|R_{21}| > 2$ , again indicating that the systematic errors are significant.

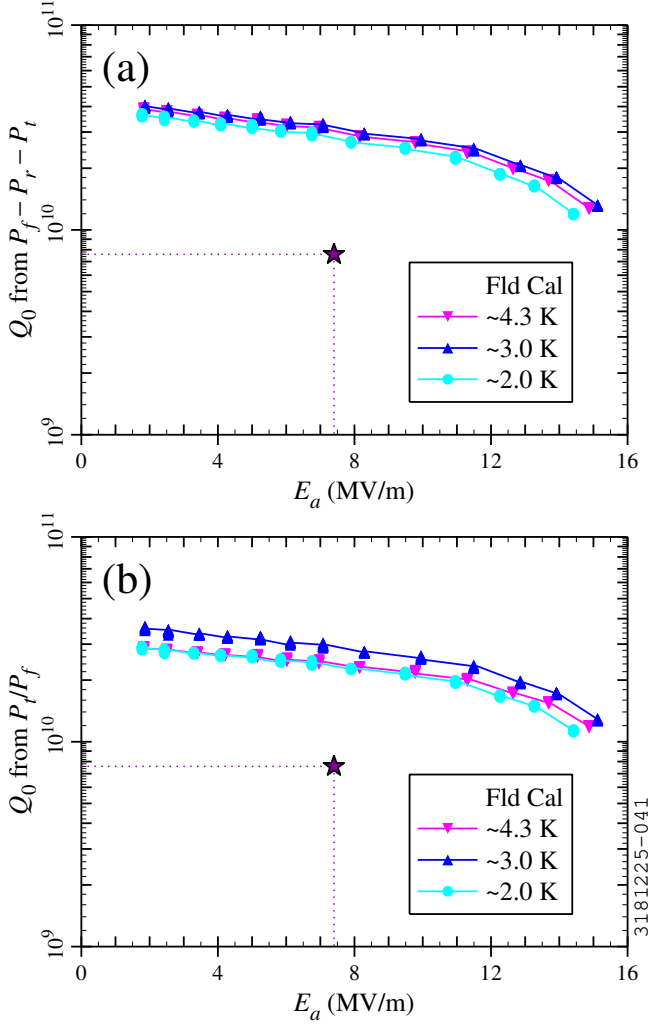


**Figure 10.** Quality factor calculated via the (a) direct method and (b) the indirect method as a function of  $E_a$  for CW measurements on a  $\beta_m = 0.54$  HWR at  $\sim 2$  K; the different curves correspond to the coupling strengths from modulated measurements at different temperatures.

Figure 11c shows results for a  $\beta_m = 0.54$  HWR cryomodule containing 8 HWRs (SCM508, tested in late February 2019). In this case, some field emission X-rays were observed for 2 out of 8 cavities. Again, some of the CW measurements were taken while conditioning the high multipacting barrier. These results show more scatter than the  $\beta_m = 0.29$  example, with less overlap between cavities than for the  $\beta_m = 0.086$  example. Some of the cavities have  $|R_{21}| > 2$ , but, fortuitously, none have  $|S_{11}| > 1$ .

It is clear from Figure 11 that, even in the most consistent cases, the systematic errors are large enough to make it impractical to obtain  $P_d$  and  $Q_0$  via the direct method. Moreover, as discussed in Section 5.3, the indirect method is impractical in the strong input coupling case. As a result,  $P_d$  and  $Q_0$  must be inferred from calorimetric measurements rather than RF power measurements for FRIB cryomodules, a situation which is not atypical for SRF cryomodules.

## 8. Conclusion

The case of continuous-wave measurements on a two-port radio-frequency cavity is considered. The assumption of a weak pickup coupler allows for simplifications, but the derivations can be generalized to the case of an arbitrary pickup coupling strength. The quality factor of the cavity can be calculated via both direct and indirect methods, the latter being possible if both coupling strengths are known. The indirect method is useful in the weak input coupling case when systematic errors are present. Graphical methods allow for rapid evaluation of the consistency of the measurements and coupling strengths, which has been found useful for both real-time feedback during cavity tests and subsequent analysis of cavity test results.

## Acknowledgments

We thank colleagues at NSCL and FRIB who have been part of the MSU SRF team over the past 25 years. FRIB SRF cavity testing is a collaborative effort between the cavity fabrication team, the cavity surface preparation team, and the FRIB cryogenics team, with support from the FRIB radio-frequency team. Thank you to David Meidlinger for typesetting the original hand-written derivations included in Section 2, Section 3.1, and Section 3.2 and sharing the source file.

This material is based upon work supported by the U.S. Department of Energy, Office of Science, Office of Nuclear Physics, and used resources of the Facility for Rare Isotope Beams (FRIB) Operations, which is a DOE Office of Science User Facility under Cooperative Agreement DE-SC0023633. Additional support was provided by the State of Michigan and Michigan State University.

## Appendix A. Analysis of Modulated Measurements

Descriptions of modulated measurements can be found in a number of textbooks, for example, Sections 8.3-8.4 of Ref. [2]. In this appendix, we first provide an overview of modulated measurements and then proceed with the assumption of a weakly-coupled pickup, which is usually a safe assumption, particularly for SRF cavities; this is an assumption made in Ref. [2]. We consider a more general analysis valid for arbitrary pickup coupling strength in Appendix A.3.

In the case of NRF cavities, frequency domain measurements are typically done in lieu of the modulated measurements (time domain) described in this section. However, the time domain discussion can be applied to the frequency domain by replacing the time-domain decay time measurement with a frequency-domain loaded bandwidth measurement; determination of the coupling in the frequency domain can be done using an  $S_{11}$  polar plot in lieu of the transient behavior of  $P_r$ .

### Appendix A.1. Modulated Measurement Basics

In contrast to the case of CW measurements with known input and pickup coupling strengths, the case of modulated measurements with unknown input and pickup coupling strengths

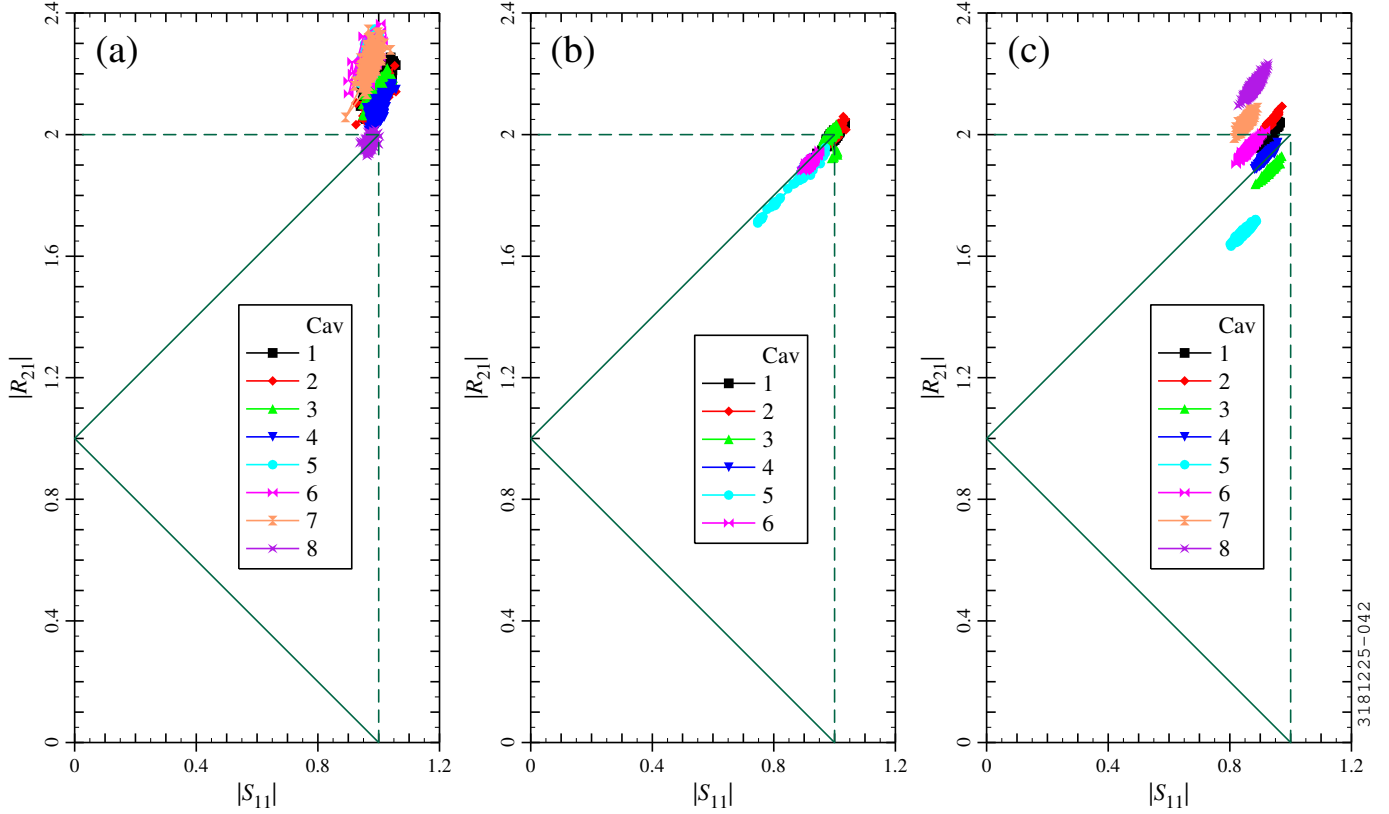


**Figure 11.** Scattering parameters for CW measurements on FRIB cryomodules: (a) a  $\beta_m = 0.086$  QWR cryomodule; (b) a  $\beta_m = 0.29$  HWR cryomodule; (c) a  $\beta_m = 0.54$  HWR cryomodule.

is not overdetermined. Hence modulated measurements do not allow for multiple methods of calculating  $Q_0$ ; likewise, values of  $|S_{11}|$  and  $|R_{21}|$  obtained from a modulated measurement will always lie on the Duality Triangle.

The goal of a modulated measurement is to obtain  $Q_0$ ,  $Q_{ext,1}$ ,  $Q_{ext,2}$ , and  $U$  from measured quantities. In a typical modulated measurement, we first measure the usual CW quantities, typically at low field:  $P_f$ ,  $P_r$ ,  $P_t$ , and  $f_0$ . Then we turn off or modulate the drive power to obtain the decay time  $\tau_L$  from the rate of decrease in  $P_t$  and calculate the loaded quality factor  $Q_L$  from  $\tau_L$ . We determine whether the cavity-input-coupler pair is undercoupled or overcoupled by comparing the reverse power upon turning on the drive power ( $P_r = P_f$  at turn-on) and turning off the drive power ( $P_r = P_e$  at turn-off): undercoupled if  $P_e < P_f$ , overcoupled if  $P_e > P_f$ .

We can calculate the CW value of  $P_d$  via Equation (11); we can then obtain  $\beta_2$  via Equation (5). The steps so far do not require any assumptions about weak pickup coupling, but the calculation of  $\beta_1$  must be done with additional care in the case of arbitrary pickup strength; we discuss the calculation of  $\beta_1$  in Appendix A.2 for the weak pickup case and Appendix A.3 for the general case. Once we have calculated  $\beta_1$ , we can obtain  $Q_0$  from  $Q_L$  by recasting Equation (8) as

$$Q_0 = Q_L (1 + \beta_1 + \beta_2). \quad (\text{A.1})$$

With  $Q_0$ ,  $\beta_1$ , and  $\beta_2$  being known, we can obtain  $Q_{ext,1}$  and

$Q_{ext,2}$  from Equation (3) and Equation (4). Finally, we can obtain  $U$  via Equation (1).

#### Appendix A.2. Weak Pickup Coupling

With the assumption that  $\beta_2 \ll 1$ , we can obtain  $\beta_1$  from  $P_f$  and  $P_r$  using Equation (16). This allows us to calculate  $Q_0$ ,  $Q_{ext,1}$ ,  $Q_{ext,2}$ , and  $U$  in a straightforward way via the steps outlined in the previous section.

#### Appendix A.3. Arbitrary Pickup Coupling Strength

In the case in which we cannot assume a weakly-coupled pickup, the cavity-input-coupler match may be affected by the pickup coupler. Let us consider the cavity and pickup coupler as a “subsystem” with quality factor  $Q_{0s}$ . We write

$$\frac{1}{Q_{0s}} = \frac{1}{Q_0} + \frac{1}{Q_{ext,2}}. \quad (\text{A.2})$$

Furthermore, let us define an “input-coupler-to-subsystem” coupling factor  $\beta_{1s}$  via

$$\beta_{1s} \equiv \frac{Q_{0s}}{Q_{ext,1}}. \quad (\text{A.3})$$

Making use of Equation (4), we can rewrite Equation (A.2) as

$$\frac{Q_0}{Q_{0s}} = 1 + \beta_2. \quad (\text{A.4})$$

Using the definitions of  $\beta_1$  and  $\beta_{1s}$  and the equation above, we can write

$$\beta_1 = \frac{Q_0}{Q_{ext,1}} = \frac{Q_{0s}}{Q_{ext,1}} \frac{Q_0}{Q_{0s}} = \beta_{1s} (1 + \beta_2). \quad (\text{A.5})$$

The case of a 2-port cavity with arbitrary coupling is considered briefly in Section 5.5 of Wangler [3]; one finding is that the condition for a matched input coupler is  $\beta_1 = 1 + \beta_2$ . Our result of  $\beta_1 = \beta_{1s}(1 + \beta_2)$  from the above equation is consistent with Wangler's result, as it implies that the matched input condition is  $\beta_{1s} = 1$ .

Using Equation (5), we can replace  $\beta_2$  with  $P_t$  (measured) and  $P_d$  (calculated from  $P_f$ ,  $P_r$ , and  $P_t$ ):

$$\beta_1 = \beta_{1s} \left( 1 + \frac{P_t}{P_d} \right). \quad (\text{A.6})$$

Considering the input coupler as being coupled to the cavity-pickup subsystem rather than just to the cavity, we rewrite Equation (16) as follows:

$$\beta_{1s} = \frac{1 \pm \sqrt{P_r/P_f}}{1 \mp \sqrt{P_r/P_f}}. \quad (\text{A.7})$$

Using the last 2 equations, we can eliminate  $\beta_{1s}$  to obtain an expression for  $\beta_1$ :

$$\beta_1 = \left( 1 + \frac{P_t}{P_d} \right) \frac{1 \pm \sqrt{P_r/P_f}}{1 \mp \sqrt{P_r/P_f}}. \quad (\text{A.8})$$

In terms of measured quantities, we can write

$$\beta_1 = \left( \frac{P_f - P_r}{P_f - P_r - P_t} \right) \frac{1 \pm \sqrt{P_r/P_f}}{1 \mp \sqrt{P_r/P_f}}. \quad (\text{A.9})$$

The equation above can be seen to be similar to Equation (16), with the distinction that we do not assume a weak pickup coupler. It is clear that it reduces to Equation (16) in the limit  $P_t \ll P_d$ . We can use this equation to calculate  $Q_0$ ,  $Q_{ext,1}$ ,  $Q_{ext,2}$ , and  $U$  for an arbitrary pickup coupler strength via the steps outlined in Appendix A.1.

## Appendix B. Analysis of CW Measurements with Arbitrary Pickup Coupling Strength

In this appendix, we consider the calculation of  $Q_0$  and the application of the Duality Triangle for cases which do not satisfy  $\beta_2 \ll 1$ . We conclude by applying these analysis techniques to the case of a cavity test in which the input and pickup coupling strengths are approximately equal.

### Appendix B.1. Direct Method

The direct method (Section 3.1) does not require any assumptions about  $\beta_2$ . Hence Equation (13) and Equation (14) are valid for arbitrary pickup coupling strength. We still need  $Q_{ext,2}$  to calculate  $U$ , so Appendix A.3 is applicable when using the direct method with arbitrary  $\beta_2$ .

### Appendix B.2. Indirect Method

We will use the “emitted wave” approach of Section 3.3 for this derivation. The same results can be obtained via the “brute force” approach of Section 3.2.

Following the “subsystem” approach of Appendix A.3, we formulate a generalized version of Equation (30) as

$$\beta_{1s} = \frac{1}{2 \sqrt{\frac{P_f}{P_e} - 1}}. \quad (\text{B.1})$$

We can eliminate  $\beta_{1s}$  using Equation (A.5) to obtain

$$\beta_1 = \frac{1 + \beta_2}{2 \sqrt{\frac{P_f}{P_e} - 1}}. \quad (\text{B.2})$$

Using Equation (3) and Equation (4) to eliminate  $\beta_1$  and  $\beta_2$ , and using Equation (33) to eliminate  $P_f/P_e$  we obtain

$$\frac{Q_0}{Q_{ext,1}} = \frac{1 + \frac{Q_0}{Q_{ext,2}}}{\frac{2}{|R_{21}|} - 1}. \quad (\text{B.3})$$

Solving for  $Q_0$ , we obtain

$$Q_0 = \frac{Q_{ext,1}}{\frac{2}{|R_{21}|} - 1 - \frac{Q_{ext,1}}{Q_{ext,2}}}. \quad (\text{B.4})$$

The above equation is valid for arbitrary  $\beta_2$  values. It is clear that it reduces to Equation (27) in the limit  $Q_{ext,2} \gg Q_{ext,1}$ . An explicit expression for  $Q_0$  in terms of measured powers and coupling strengths is

$$Q_0 = \frac{Q_{ext,1}}{2 \sqrt{\frac{Q_{ext,1}}{Q_{ext,2}} \cdot \frac{P_f}{P_t}} - 1 - \frac{Q_{ext,1}}{Q_{ext,2}}}. \quad (\text{B.5})$$

Likewise, an expression for  $P_d$  in terms of measured powers and coupling strengths is

$$P_d = P_t \frac{Q_{ext,2}}{Q_{ext,1}} \left( 2 \sqrt{\frac{Q_{ext,1}}{Q_{ext,2}} \cdot \frac{P_f}{P_t}} - 1 - \frac{Q_{ext,1}}{Q_{ext,2}} \right), \quad (\text{B.6})$$

and a corresponding expression in terms of  $|R_{21}|$  and  $P_f$  is

$$P_d = |R_{21}| \left[ 2 - |R_{21}| \left( 1 + \frac{Q_{ext,1}}{Q_{ext,2}} \right) \right] P_f. \quad (\text{B.7})$$

### Appendix B.3. Graphical Assessment Method

The Duality Triangle derivation of Section 4 made use of Equation (17) and Equation (26), both equations for  $\beta_1$ . Analogous equations valid for arbitrary  $\beta_2$  are Equation (A.7), which can be rewritten as

$$\beta_{1s} = \frac{1 \pm |S_{11}|}{1 \mp |S_{11}|} \quad (\text{B.8})$$

and Equation (B.1), which can be rewritten as

$$\beta_{1s} = \frac{1}{\frac{2}{|R_{21}|} - 1} = \frac{|R_{21}|}{2 - |R_{21}|}. \quad (\text{B.9})$$

Elimination of  $\beta_{1s}$  once again leads us to Equation (36), which we can see to be valid for arbitrary  $\beta_2$ . Hence, provided  $Q_{ext,1}$  and  $Q_{ext,2}$  are calculated correctly (per Appendix A), the Duality Triangle can be applied for arbitrary pickup coupling strength.

#### Appendix B.4. Example: Cold Test with Approximately Equal Input and Pickup Coupling Strengths

A recent cold test with a pickup coupler of coupling strength similar to that of the input coupler can serve to illustrate the analysis methods described above. The coupling strengths calculated from modulated measurements at about 2 K are shown in [Table B.2](#). Given that  $Q_0$  is of order  $1 \cdot 10^{10}$  near 2 K, it is clear that the usual assumption of  $\beta_2 \ll 1$  cannot be justified. The assumption of weak pickup coupling leads to significantly different values for the coupling strengths relative to the values obtained with the more general approach of [Appendix A.3](#).

**Table B.2.** Calculated coupling strength values from modulated measurements on a  $\beta_m = 0.65$  cavity with different assumptions.

Pickup coupling strength	$Q_{ext,1}$	$Q_{ext,2}$
Assume weak	$4.10 \cdot 10^{10}$	$1.72 \cdot 10^{10}$
Arbitrary	$2.26 \cdot 10^{10}$	$2.12 \cdot 10^{10}$

The discrepancy can be seen clearly via the Duality Triangle, as illustrated in [Figure B.12](#), which shows CW measurements taken while pumping on the bath to reduce the temperature from 4.3 K to 2 K (green diamonds) as well as some measurements before and after the pump-down (red squares, blue triangles). When the coupling strengths are calculated with the weak pickup assumption (per [Appendix A.2](#)), the measured CW values do not fall on the sides of the Duality Triangle ([Figure B.12a](#)), indicating that the calculated value of  $Q_{ext,2}/Q_{ext,1}$  is inconsistent with the measured values of  $P_f$ ,  $P_r$ , and  $P_t$ . When the coupling strengths are calculated without assuming a weak pickup (per [Appendix A.3](#)), the results are approximately consistent with the Duality Triangle, with the measured values all having  $\beta_1 < 1$  ([Figure B.12b](#)).

Corresponding quality factors as a function of temperature and field are shown in [Figure B.13](#). Curves on the left-hand side assume weak pickup coupling for both the calculation of the coupling strengths and the indirect calculation of  $Q_0$ . The discrepancy in  $Q_0$  values between the direct method (dark colors) and indirect method (light colors) is significant.

Curves on the right-hand side of [Figure B.13](#) allow for an arbitrary pickup coupling strength for the analysis of the modulated measurements and the indirect calculation of  $Q_0$ . The agreement between  $Q_0$  values from the direct and indirect method is significantly improved, though not perfect. As seen in [Figure B.13](#), wrongly assuming weak coupling causes us to infer a significantly lower value for the indirect  $Q_0$ . The weak pickup coupling assumption mistakenly considers the power transferred to the pickup coupler to be dissipated in the cavity, thereby mistakenly finding a lower value of  $Q_0$ .

## References

- [1] E. L. Ginzton, *Microwave Measurements*, McGraw-Hill, New York, 1957.
- [2] H. Padamsee, J. Knobloch, T. Hays, *RF Superconductivity for Accelerators*, John Wiley & Sons, New York, 1998.
- [3] T. P. Wangler, *RF Linear Accelerators*, 2nd ed., Wiley-VCH, Weinheim, Germany, 2008.
- [4] J. P. Holzbauer, Y. Pischnikov, D. A. Sergatskov, W. Schappert, S. Smith, Systematic uncertainties in RF-based measurement of superconducting cavity quality factors, *Nucl. Instrum. Methods Phys. Res. A* 830 (2016) 22–29. doi:[10.1016/j.nima.2016.05.025](https://doi.org/10.1016/j.nima.2016.05.025).
- [5] J. P. Holzbauer, C. Contreras, Y. Pischnikov, D. Sergatskov, W. Schappert, Improved RF measurements of SRF cavity quality factors, *Nucl. Instrum. Methods Phys. Res. A* 913 (2019) 7–14. doi:[10.1016/j.nima.2018.09.155](https://doi.org/10.1016/j.nima.2018.09.155).
- [6] W. Hartung, et al., Superconducting coaxial resonator development for ion linacs at Michigan State University, in: *Proc. Linac 2010: XXV Linear Accelerator Conference*, Tsukuba, Japan, THP039, 2011, pp. 845–847. URL: <https://jacow.org/LINAC2010/papers/THP039.pdf>.
- [7] T. Xu, et al., Completion of FRIB Superconducting Linac and Phased Beam Commissioning, in: *Proc. SRF 2021: 20th Int. Conf. RF Supercond., Virtual Conference, MOOFAV10*, 2022, pp. 197–202. doi:[10.18429/JACoW-SRF2021-MOOFAV10](https://doi.org/10.18429/JACoW-SRF2021-MOOFAV10).
- [8] C. Zhang, W. Hartung, J. Popielarski, K. Saito, S.-H. Kim, W. Chang, T. Xu, Certification testing of production superconducting quarter-wave and half-wave resonators for FRIB, *Nucl. Instrum. Methods Phys. Res. A* 1014 (2021) 165675. doi:[10.1016/j.nima.2021.165675](https://doi.org/10.1016/j.nima.2021.165675).
- [9] K. McGee, et al., Advanced surface treatments for medium-velocity superconducting cavities for high-accelerating gradient continuous-wave operation, *Nucl. Instrum. Methods Phys. Res. A* 1059 (2024) 168985. doi:[10.1016/j.nima.2023.168985](https://doi.org/10.1016/j.nima.2023.168985).
- [10] W. Hartung, W. Chang, K. Elliott, S. Kim, T. Konomi, K. Saito, P. Tutt, T. Xu, Investigation of plasma processing for coaxial resonators, in: *Proc. SRF 2023: 21st Int. Conf. RF Superconductivity*, Grand Rapids, MI, USA, JACoW, 2023, pp. 960–967. doi:[10.18429/JACoW-SRF2023-THIXA01](https://doi.org/10.18429/JACoW-SRF2023-THIXA01).
- [11] W. Hartung, W. Chang, Y.-L. Cheon, K. Elliott, S.-H. Kim, T. Konomi, P. Tutt, Y. Wu, T. Xu, Report on first plasma processing trial for a FRIB quarter-wave resonator cryomodule, *Technical Report arXiv:2511.06732, arXiv.org*, 2025. doi:[10.48550/arXiv.2511.06732](https://doi.org/10.48550/arXiv.2511.06732).
- [12] D. J. Meidlinger, *Design, Fabrication and Testing of Superconducting RF Cavities for High Average Beam Currents*, Ph.D. thesis, Department of Physics and Astronomy, Michigan State University, East Lansing, Michigan, USA, 2007.

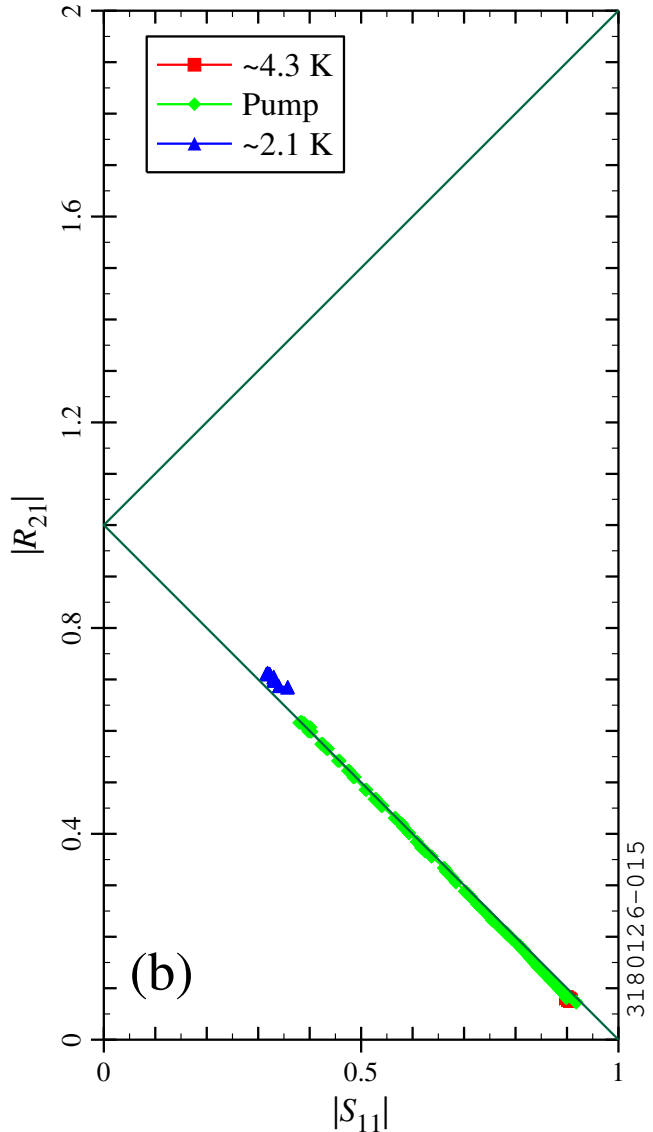
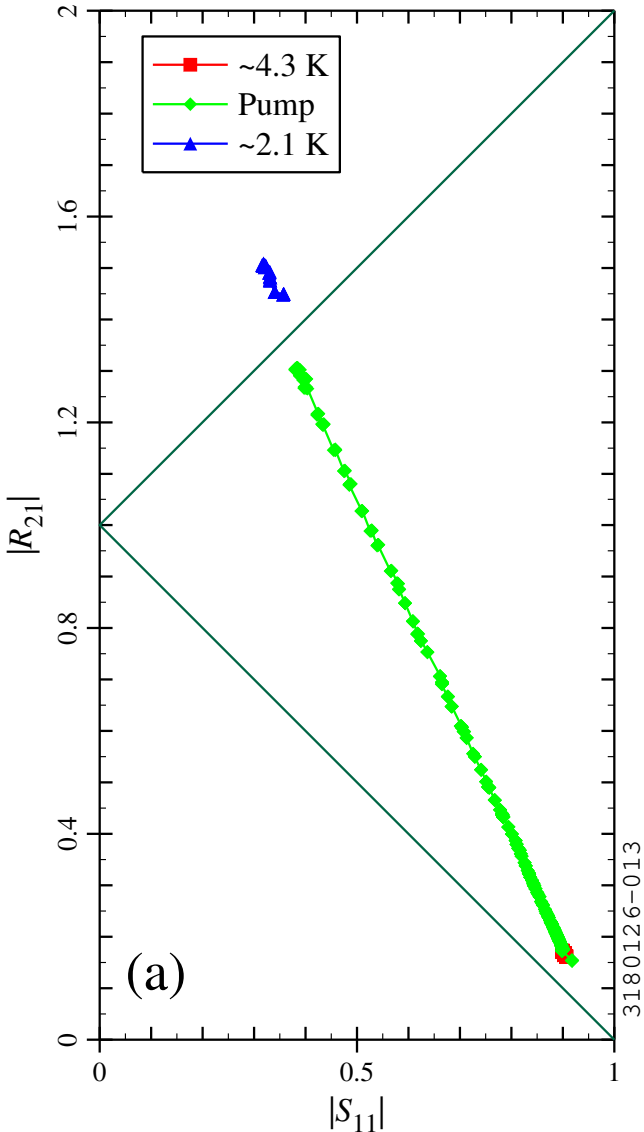


**Figure B.12.** Duality Triangle for a cold test on a cavity with approximately matched pickup coupling (S65-004, tested in October 2024). Coupling strengths are obtained from modulated measurement (a) assuming or (b) not assuming a weak pickup.

- [13] T. Powers, Theory and practice of cavity RF test systems, in: Proc. SRF 2005: 12th Int. Workshop RF Supercond., Ithaca, NY, USA, SUP02, 2005, pp. 40–70. URL: <https://jacow.org/SRF2005/papers/SUP02.pdf>.
- [14] K. Halbach, R. F. Holsinger, SUPERFISH—a computer program for evaluation of RF cavities with cylindrical symmetry, Part. Accel. 7 (1976) 213–222.
- [15] J. H. Billen, L. M. Young, POISSON/SUPERFISH on PC compatibles, in: Proc. PAC 1993: 15th Part. Accel. Conf., Washington DC, USA, IEEE, Piscataway, New Jersey, 1993, pp. 790–792. URL: [https://jacow.org/p93/PDF/PAC1993\\_0790.PDF](https://jacow.org/p93/PDF/PAC1993_0790.PDF).
- [16] D. G. Myakishev, V. P. Yakovlev, An interactive code SUPERLANS for evaluation of RF-cavities and acceleration structures, in: Proc. PAC 1991: 14th Part. Accel. Conf., San Francisco, CA, USA, IEEE, Piscataway, New Jersey, 1991, pp. 3002–3004. URL: [https://jacow.org/p91/PDF/PAC1991\\_3002.PDF](https://jacow.org/p91/PDF/PAC1991_3002.PDF).
- [17] U. Becker, CST’s commercial beam-physics codes, 2006. URL: [https://jacow.org/icap06/TALKS/THM2IS03\\_TALK.PDF](https://jacow.org/icap06/TALKS/THM2IS03_TALK.PDF), presented at ICAP 2006: 9th International Computational Accelerator Physics Conference (02–06 Oct 2006, Chamonix Mont-Blanc, France), THM2IS03.
- [18] O. Kononenko, L. Ge, C. Ko, Z. Li, C.-K. Ng, L. Xiao, Advances in Massively Parallel Electromagnetic Simulation Suite ACE3P, in: Proc. ICAP 2015: 12th Int. Computational Accel. Phys. Conf., Shang-

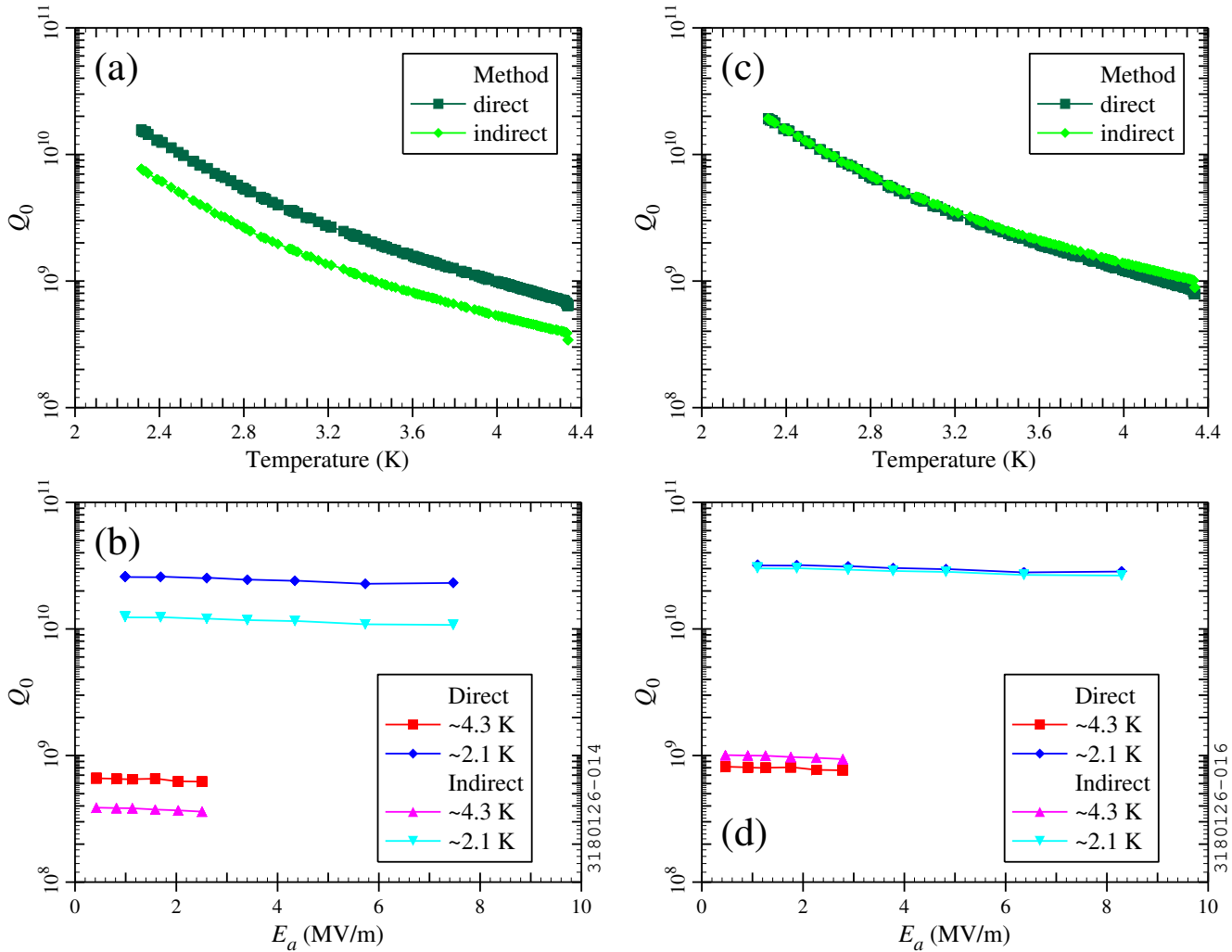


**Figure B.13.** Calculated quality factor as a function of (a, c) temperature and (b, d) accelerating gradient ( $E_a$ ) for the cavity test with approximately matched pickup coupling. Coupling strengths and indirect  $Q_0$  values are calculated (a, b) assuming or (c, d) not assuming a weak pickup.

hai, China, FRAJ13, 2016, pp. 183–187. doi:[10.18429/JACoW-ICAP2015-FRAJ13](https://doi.org/10.18429/JACoW-ICAP2015-FRAJ13).

- [19] S. Zhao, W. Chang, S. Kim, H. Maniar, D. Morris, P. Ostroumov, J. Popielarski, H. Ren, N. Usher, The LLRF control design and validation at FRIB, in: Proc. NAPAC 2019: North American Particle Accelerator Conf., Lansing, MI, USA, JACoW, 2019, pp. 667–669. doi:[10.18429/JACoW-NAPAC2019-WEPLM03](https://doi.org/10.18429/JACoW-NAPAC2019-WEPLM03).
- [20] W. Chang, et al., Bunker testing of FRIB cryomodules, in: Proc. NAPAC 2019: North American Particle Accelerator Conf., Lansing, MI, USA, JACoW, 2019, pp. 765–767. doi:[10.18429/JACoW-NAPAC2019-WEPLM73](https://doi.org/10.18429/JACoW-NAPAC2019-WEPLM73).